Comparison of Turbulence Modeling Strategies for Indoor Flows

Ammar M. Abdilghanie

Lance R. Collins

David A. Caughey[1]
e-mail: dac5@cornell.edu

Sibley School of Mechanical & Aerospace Engineering,
Cornell University,
Ithaca, NY 14853-7501

Turbulence modeling techniques are compared for the simulation of low speed indoor air flow in a simple room. The effect of inlet turbulence intensity on the flow field is investigated using the constant coefficient large eddy simulation (LES) model with uniform mean inlet conditions at several levels of inlet turbulence intensities. The results show significant differences between the simulations with laminar inflow conditions and those in which turbulence was introduced at the inlet. For simulations with turbulent inlet conditions, it is noticed that the jet transitions to a state of fully developed turbulence wherein the dynamics of the flow become nearly insensitive to any further increase in the level of inlet turbulence. For laminar flow conditions, it is seen that the jet slowly spreads and mixes with the quiescent room air. As a result, the jet reaches a fully developed turbulent state further away from the inlet relative to the simulations with inlet turbulence. The effect of using experimental inlet profiles is also investigated. It is seen that, close to the inlet, the flow is sensitive to the inflow details, whereas further away from the inlet, these effects become less pronounced. The results from the constant coefficient and the dynamic LES models are compared. The most noticeable differences in the flow occur at the locations where the subgrid-scale's contribution to the turbulent kinetic energy is highest. Finally, the results from the dynamic LES and the k-ϵ models are compared. It is found that there are significant differences between the two models for the zero inlet turbulence limit where the flow is most probably transitional in nature and turbulence has not yet reached a fully developed state. It is seen that in the laminar inflow case the k-ϵ model predicts a fully turbulent jet very close to the inlet and thus fails to capture the slow development of the jet found in LES. Accordingly, the k-ϵ model results are nearly insensitive to the level of inlet turbulence especially far from the origin of the flow. It is also seen that for cases with nonzero inlet turbulence level, the k-ϵ model predicts the general features of the mean flow reasonably well; however, the k-ϵ model overpredicts the jet spreading rate and the turbulent kinetic energy close to the inlet. Furthermore, the k-ϵ model under predicts the turbulence level near the corner of the ceiling as it fails to capture the complicated mean velocity and turbulent kinetic energy, most likely because of the highly intermittent flow pattern found there in LES. [DOI: 10.1115/1.3112386]

1 Introduction

The vast majority of ventilation systems are designed assuming the pollutants and the ventilating air are well mixed within a room, regardless of its size. In many instances, this is far from reality. There are numerous cases where the dispersion of pollutants does not correspond to a well-mixed condition [1]. Computational fluid dynamics (CFD) provides a practical option for predicting the airflow and pollutant distributions in buildings. CFD can be used to determine the best locations of air supply diffusers and return outlets and the flow rate needed to create an acceptable indoor air quality.

The Reynolds number for the flow inside a built environment is most likely high; hence the CFD model must account for turbulence. Turbulence modeling can be done at a variety of levels, depending on accuracy requirements, the computational facilities, and the wall-clock time available for the calculation. Direct numerical simulation (DNS) is a model-free approach that involves obtaining the three-dimensional solution of the Navier–Stokes (NS) equations with full resolution of all of the spatial and temporal scales of the turbulent motion. With DNS, the complete flow field throughout the domain is determined with no modeling assumptions, and thus it offers the most accurate characterization of the turbulence possible. The principal drawback of DNS is that its computational cost increases in proportion to the cube of the Reynolds number [2]. This limits its use mainly to fundamental scientific investigations of turbulence, and makes it impractical for CFD of the sort required for the present application.

At the other extreme in terms of computational cost is the Reynolds-averaged Navier–Stokes (RANS) modeling. With RANS, modeled equations for the mean velocity of a statistically stationary turbulent flow are solved. The higher-order Reynolds stresses are usually obtained from a turbulent viscosity model, which is algebraically related to other turbulence quantities such as the turbulent kinetic energy k and energy dissipation rate ϵ for which modeled transport equations are solved. Because RANS is not concerned with solving for the fluctuating velocity and pressure fields, the computational cost is much lower (by orders of magnitude) than the equivalent DNS. However, the accuracy of RANS predictions is limited by the fidelity of the closure models used to represent the effects of the turbulent fluctuations. Despite decades of research, there remain fundamental limitations to what can be expected from a RANS simulation [3].

Large eddy simulation (LES) has emerged as an important intermediate approach, whereby one solves for the instantaneous filtered velocity of the largest energy-containing eddies of the turbulent motion and models the effect of the subgrid-scale motions

[1]Corresponding author. Present address: Department of Mechanical & Aerospace Engineering, Cornell University, 248 Upson Hall, Ithaca, NY 14853-7501.

Contributed by the Fluids Engineering Division of ASME for publication in the JOURNAL OF FLUIDS ENGINEERING DIVISION. Manuscript received June 14, 2008; final manuscript received March 8, 2009; published online April 15, 2009. Review conducted by Paul Durbin.

on the resolved scales. As LES directly solves for the large-scale turbulence, it yields more accurate results than RANS, yet has a much lower computational cost than DNS, in which all of the scales of the turbulence must be fully resolved. With the rapid growth in computer speed and memory over the past 30 years, LES has moved from being a research tool to a valuable tool for studying flows in realistic geometries.

The development of LES for turbulent flows has been an active area of research, and there have been several important advances in LES since the pioneering work of Smagorinsky [4], Lilly [5], Deardorff [6], Schumann [7], and others. Advances have been made in (i) modeling the unresolved processes; (ii) accurate numerical methods on structured and unstructured grids; (iii) detailed comparison of LES calculations with DNS and experimental data in canonical flows; (iv) extensions to include additional phenomena, e.g., turbulent combustion; and (v) computational power, which has increased by more than four orders of magnitude since the 1970s [8]. Various subgrid-scale (SS) models have been developed, beginning with the early work that relied on an eddy viscosity model with a constant coefficient C_s, which is a function of the flow regime [4–6]. The dynamic model was first introduced by Germano et al. [9], with important modifications and extensions provided by Lilly [10] and Meneveau et al. [11]. The dynamic model provides a method for estimating the Smagorinsky coefficient locally. It has proven quite successful, and the same procedure has been applied in several other contexts [2]. One requirement for truly accurate LES is that the grid adequately resolve the largest energy-containing eddies so that the subgrid model is subdominant to the resolved scales. This implies either having some a priori knowledge of the length scales of the turbulence so that the grid can be designed accordingly or having an adaptive approach that refines the grid where needed.

In the field of indoor air flow simulation, several researchers have studied the performance of the k-ϵ-model [12,13]. The authors demonstrated that the model can successfully predict the mean velocities. Chen [14] compared the performance of four different k-ϵ and Reynolds stress models (RSMs) for four common problems in air flows: natural convection, forced convection, mixed convection, and impinging jet flows. The study showed that all four models predicted the mean velocities reasonably well; however, they failed to accurately predict the turbulence levels. While RANS models are strictly applicable to fully developed turbulent flows [15], it is not uncommon in indoor air flows, especially at low ventilation rates, to have laminar, transitional, and slowly developing turbulent flows co-existing [15,16].

LES has been successfully applied to airflow simulations [17–19]. Davison and Nielson [17] compared the performance of the standard Smagorinisky and dynamic models for a simply ventilated room. It was found that the dynamic model agrees better with the experimental data. Jiang et al. [19] used LES to study air flows in and around buildings. They compared the Smagorinsky SS model, the filtered dynamic (FD) model by Zhang and Chen [20], and the stimulated small-scale subgrid-scale (SSS) model by Shah and Ferziger [21]. They concluded that the simple SS model gives less accurate results in regions where the flow is not fully developed, as compared with the FD and the SSS models. The SS model was found to work fairly well for the outdoor flows, where conditions are fully turbulent. Since the FD and the SSS models are computationally more intensive, the SS model was recommended for outdoor flows and the SSS and FD models were recommended for indoor flows. This represented an optimum solution to ensure accurate representation of upstream conditions.

Recently, Zhai et al. [22] and Zhang et al. [23] compared eight different RANS and LES models for simulation of representative indoor air flows such as forced and mixed convection in ventilated spaces and natural convection in a tall cavity. They concluded that the v2f-dav model by Davidson et al. [24] and LES are the most suitable models in predicting air velocity, temperature, and turbulent quantities for low Rayleigh number natural convection flows. In forced convection with low turbulence levels, the renormalization group (RNG) k-ϵ model by Yakhot and Orszag [25], the low Reynolds number k-ϵ model due to Launder and Sharma LRN-LS [26], the v2f-dav, and LES all performed very well. The v2f model by Durbin [27] was found to be very promising but the numerical algorithm has to be constructed so as to avoid some inherent numerical problems. The RSMs were shown to be able to capture more flow details than eddy viscosity based models; however, they require more computational time. The authors concluded that LES provided more detailed and possibly more accurate predictions for indoor air flows and that it is a very important tool for understanding the dynamics of indoor airflow.

In the current investigation, we use LES to model the air flow inside an experimental flow chamber located in the Indoor-Flow-Laboratory (IFL) at Syracuse University. The hydrodynamic conditions within the facility are typical of displacement ventilation systems, where the supply air displaces the room air with presumed minimal mixing so as to achieve a high air change efficiency [1].

Consistent with the incremental procedure for simulation of displacement ventilation systems laid out by Chen and Srebric [28] and Chen and Zhai [29], we have neglected thermal convection effects and geometrical complexities at this stage. The main objective here was limited to modeling and understanding the basic flow behavior inside the IFL, with an eye toward incorporating more comprehensive physics and more geometrical details in future investigations.

The sensitivity of the flow field to the inlet turbulence levels and the details of the flow at the inlet are investigated. The performance of the Smagorinsky LES model with constant coefficient and the dynamic model in predicting the air flow are systematically studied and analyzed. Finally, light is shed on the performance of the k-ϵ model in predicting the mean flow and the turbulent kinetic energy throughout the flow field at varying inlet turbulence levels.

2 Turbulence Models

2.1 RANS Equations. The ensemble average of the constant density NS equations takes the form [30]

$$\frac{\partial \rho}{\partial t} + \frac{\partial \rho \bar{u}_i}{\partial x_i} = 0 \tag{1}$$

$$\frac{\partial \rho \bar{u}_i}{\partial t} + \frac{\partial}{\partial x_j}(\rho \bar{u}_i \bar{u}_j) = -\frac{\partial \bar{p}}{\partial x_i} + \frac{\partial}{\partial x_j}\left[\mu\left(\frac{\partial \bar{u}_i}{\partial x_j} + \frac{\partial \bar{u}_j}{\partial x_i} - \frac{2}{3}\frac{\partial \bar{u}_l}{\partial x_l}\delta_{ij}\right)\right] + \frac{\partial}{\partial x_j}(-\rho\overline{u_i' u_j'}) \tag{2}$$

where ρ is the density, p is the pressure, μ is the dynamic viscosity, $\bar{u}_i$ is the velocity component in the x_i direction, and the overbar indicates an averaged quantity. The symbol δ_{ij} denotes the Kronecker delta, and the Einstein summation convention is used. The Reynolds-averaged approach to turbulence modeling requires that the Reynolds stress term $-\rho\overline{u_i' u_j'}$ be appropriately modeled. In the k-ϵ model, the Boussinesq approximation is used to relate the Reynolds stresses to the mean velocity gradients through

$$-\rho\overline{u_i' u_j'} = \mu_t\left(\frac{\partial \bar{u}_i}{\partial x_j} + \frac{\partial \bar{u}_j}{\partial x_i}\right) - \frac{2}{3}\left(\rho k + \mu_t \frac{\partial \bar{u}_k}{\partial x_k}\right)\delta_{ij} \tag{3}$$

where the turbulent (or eddy) viscosity μ_t must be specified in order for the above system of equations to be closed.

2.1.1 The Standard k-ϵ Model. The simplest complete models of turbulence are two-equation models in which the solution of two separate transport equations allows the turbulent velocity and length scales to be independently determined. According to Ref. [30], the standard k-ϵ model in FLUENT falls within this class of turbulence models that has become the workhorse of practical

engineering flow calculations in the time since it was proposed by Launder and Spalding [31]. The turbulence kinetic energy k and its rate of dissipation ϵ are obtained from the following transport equations:

$$\frac{\partial \rho k}{\partial t} + \frac{\partial}{\partial x_i}(\rho k \bar{u}_i) = \frac{\partial}{\partial x_j}\left[\left(\mu + \frac{\mu_t}{\sigma_k}\right)\frac{\partial k}{\partial x_j}\right] + G_k - \rho\epsilon \tag{4}$$

$$\frac{\partial \rho \epsilon}{\partial t} + \frac{\partial}{\partial x_i}(\rho \epsilon \bar{u}_i) = \frac{\partial}{\partial x_j}\left[\left(\mu + \frac{\mu_t}{\sigma_\epsilon}\right)\frac{\partial \epsilon}{\partial x_j}\right] + C_{1\epsilon}\frac{\epsilon}{k}G_k - C_{2\epsilon}\rho\frac{\epsilon^2}{k} \tag{5}$$

where G_k represents the generation of turbulence kinetic energy due to the mean velocity gradients, and $C_{1\epsilon}$, and $C_{2\epsilon}$ are the model constants. The details of how these terms are calculated in FLUENT can be found in Ref. [30] and are omitted here for the sake of brevity. In these equations, σ_k and σ_ϵ are the turbulent Prandtl numbers for k and ϵ, respectively. The turbulent viscosity μ_t is computed by combining k and ϵ as follows:

$$\mu_t = \rho C_\mu \frac{k^2}{\epsilon} \tag{6}$$

The model constants $C_{1\epsilon}$, $C_{2\epsilon}$, C_μ, σ_k, and σ_ϵ have the following default values: $C_{1\epsilon}=1.44$, $C_{2\epsilon}=1.92$, $C_\mu=0.09$, $\sigma_k=1.0$, and $\sigma_\epsilon=1.3$.

2.1.2 A Two-Layer Model for the Enhanced Wall Treatment. The two-layer approach is an integral part of the enhanced wall treatment and is used to specify both ϵ and the turbulent viscosity in the near-wall cells [30]. In this approach, the whole domain is subdivided into a viscosity-affected region and a fully turbulent region. The demarcation between the two regions is determined by a wall-distance-based, turbulent Reynolds number Re_y. In the fully turbulent region ($\mathrm{Re}_y > \mathrm{Re}_y^*$), the k-ϵ model described above is employed. In the viscosity-affected near-wall region ($\mathrm{Re}_y < \mathrm{Re}_y^*$), the one-equation model of Wolfshtein [32] is employed. Here the default value of $\mathrm{Re}_y^*=200$ is used. In the enhanced wall treatment approach, the turbulent viscosity is smoothly blended with the high-Reynolds-number μ_t definition from the outer region. The main purpose of the blending function is to allow convergence even when the k-ϵ solution in the outer layer does not match the two-layer formulation [30]. In the enhanced wall function approach, FLUENT blends the linear (laminar) and the logarithmic (turbulent) laws-of-the-wall for the mean velocity using a function suggested by Kader [33] to form a single law-of-the-wall for the entire wall region. The resulting law-of-the-wall has the correct asymptotic behavior in the viscous sublayer and the log-law region and also represents the velocity profile in the wall buffer region reasonably well [30]. The k equation is solved in the whole domain including the wall-adjacent cells. The boundary condition for k imposed at the wall is

$$\frac{\partial k}{\partial n} = 0 \tag{7}$$

where n is the local coordinate normal to the wall. As we will illustrate, the dynamics of the flow are dominated by the shear layers and hence we expect the flow to be relatively insensitive to the boundary conditions applied at the walls.

2.2 LES Equations. By filtering the constant density NS equations, one obtains [30]

$$\frac{\partial \rho}{\partial t} + \frac{\partial \rho \tilde{u}_i}{\partial x_i} = 0 \tag{8}$$

$$\frac{\partial \rho \tilde{u}_i}{\partial t} + \frac{\partial}{\partial x_j}(\rho \tilde{u}_i \tilde{u}_j) = \frac{\partial}{\partial x_j}\left(\frac{\partial \sigma_{ij}}{\partial x_j}\right) - \frac{\partial \tilde{p}}{\partial x_i} - \frac{\tau_{ij}}{\partial x_j} \tag{9}$$

where the tilde indicates a filtered quantity,

$$\sigma_{ij} = \mu\left(\frac{\partial \tilde{u}_i}{\partial x_j} + \frac{\partial \tilde{u}_j}{\partial x_i}\right) - \frac{2}{3}\mu\frac{\partial \tilde{u}_l}{\partial x_l}\delta_{ij} \tag{10}$$

that represents the contributions of the filtered velocity to the viscous stress tensor, and τ_{ij} is the subgrid-scale stress defined by

$$\tau_{ij} \equiv \widetilde{\rho u_i u_j} - \rho \tilde{u}_i \tilde{u}_j \tag{11}$$

The subgrid stresses are modeled using the Boussinesq approximation as in the RANS models:

$$\tau_{ij} - \tfrac{1}{3}\tau_{kk}\delta_{ij} = -2\mu_t \tilde{S}_{ij} \tag{12}$$

where $\tilde{S}_{ij}$ is the rate-of-strain tensor for the filtered velocity, defined by

$$\tilde{S}_{ij} \equiv \frac{1}{2}\left(\frac{\partial \tilde{u}_i}{\partial x_j} + \frac{\partial \tilde{u}_j}{\partial x_i}\right) \tag{13}$$

and μ_t is the subgrid-scale turbulent (or eddy) viscosity.

2.2.1 Smagorinsky-–Lilly Model. In the Smagorinsky model, the eddy viscosity is modeled by

$$\mu_t = \rho L_s^2 |\tilde{S}| \tag{14}$$

where L_s is the mixing length for the subgrid scales and $|\tilde{S}| \equiv \sqrt{2\tilde{S}_{ij}\tilde{S}_{ij}}$. In FLUENT, L_s is computed using

$$L_s = \min(\kappa d, C_s V^{1/3}) \tag{15}$$

where $\kappa(=0.41)$ is the von Karman constant, d is the distance to the closest wall, and V is the volume of the computational cell. A value of 0.1 for C_s has been found satisfactory for a wide range of flows and was thus used in the current investigation.

2.2.2 Dynamic Smagorinsky–Lilly Model. Germano et al. [9] and subsequently Lilly [10] conceived a procedure by which the Smagorinsky model constant C_s is dynamically computed based on the information provided by the resolved scales of motion. They realized that the LES equations are solved for the filtered velocity field, although this filtering is not always explicitly performed. Using single- and double-filtered residual stress tensors, Germano [34] derived a closed expression for a tensor referred to as the *resolved stress* tensor, in terms of the grid-filtered velocity field. The resolved stress tensor can be loosely interpreted as the contribution to the residual stress from the largest unresolved scales [2]. If a Smagorinsky type model for the deviatoric part of this tensor is constructed, then an adjustable coefficient C_s can be locally matched to provide the best estimate for the deviatoric part of the resolved stress tensor. As it is impossible to match the five independent components of the deviatoric tensor, Lilly [10] derived a specification of C_s that minimizes the mean-square error. In the implementation of the dynamic LES model in FLUENT, C_s is clipped at zero and 0.23 by default to eliminate backscatter and to avoid numerical instabilities [30].

3 Numerical Solution Details

The commercial CFD code FLUENT was used to simulate the flow. The temporally second-order accurate, unsteady solver based on the noniterative time advancement algorithm was used with the incompressible pressure-based segregated solver, using the pressure-implicit with splitting of operator pressure-velocity coupling scheme. The central differencing scheme is an ideal choice for LES because of its low numerical diffusion; however, it can result in unphysical oscillations in the solution. This situation is worsened if combined with the low subgrid-scale turbulent diffusivity used in LES. The bounded central differencing scheme is a composite normalized variable diagram scheme that consists of pure central differencing, a blended scheme of the central differencing and the second-order upwind scheme, and the first-order upwind scheme, which is used only when the convection bound-

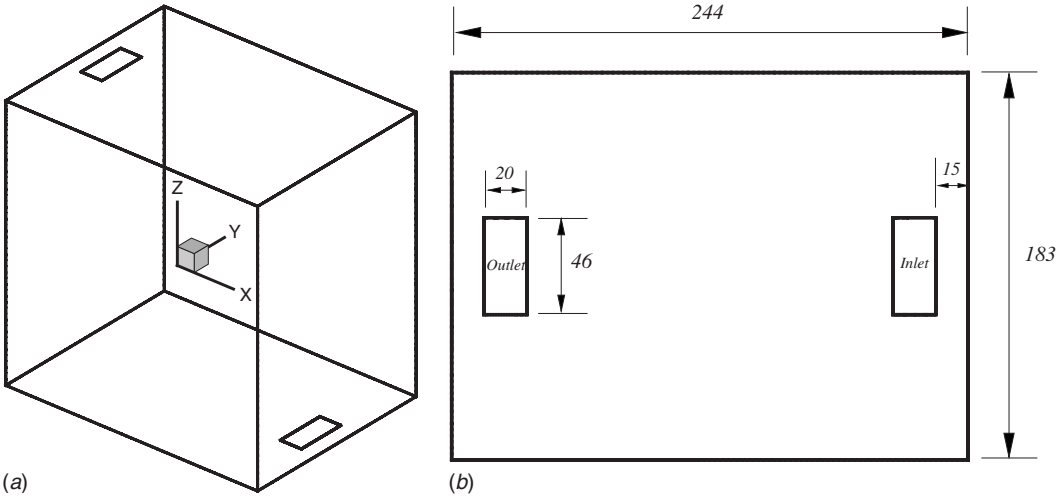

Fig. 1 (*a*) **Geometry of Indoor Flowfield Laboratory Chamber; dimensions are 244×183×244 cm³.** (*b*) **Top view; dimensions are in cm.**

edness criterion is violated [30]. Provided that the numerical solution converges, this approach leads to pure second-order differencing [30]. The bounded central difference scheme was used for discretization of both the pressure and momentum equations, and default tolerances were used (a residual tolerance of 0.0001 and relaxation factors of 1 for the pressure and momentum equations). Air with constant density and viscosity at standard sea level conditions was used. The time step was set so that the resulting maximum Courant number would be no larger than 0.5. The boundary conditions used in the first stage of this investigation were simple plug/uniform flow velocity profile at the inlet, with uniform turbulence intensities of 0%, 5%, and 13%, a uniform turbulence length scale equal to 7% of the inlet hydraulic diameter, a pressure outlet for the outflow, and solid wall boundary conditions everywhere else. Simulations of the flow were continued up to the time when the flow was approximately statistically stationary. In the second stage of the study, the inlet velocity and turbulence profiles obtained from experiments conducted in the IFL at Syracuse University [35] were used in the simulations.

3.1 Description of the Geometry. The IFL chamber consists of a $2.44\times1.83\times2.44$ m^3 cubicle, with optical access for particle image velocimetry (PIV) measurements through the front (1.83×2.44 m^2) wall. The origin of the coordinate system is located at the center of the cubicle, with positive z pointing vertically upward and positive x pointing toward the front wall (see Fig. 1). The chamber half-height L is used to nondimensionalize the vertical distance. The chamber is designed to represent a typical indoor-flow environment for a single occupancy cubicle. An isometric view of the chamber is shown in Fig. 1(*a*) and a top view is shown in Fig. 1(*b*). The cubicle is ventilated by a low speed, closed-loop system that is designed to allow an occupant's thermal plume to be a significant factor in driving the flow. There is a 0.2×0.46 m^2 inlet on the floor, near the front wall, and an identically sized outlet in the ceiling near the rear wall. The average inlet and outlet flow velocity is 0.2 m/s.

3.2 Description of the Computational Grid. An initial grid containing $48\times32\times48$ cells was developed using FLUENT's Gambit mesh generator to represent the chamber. The accuracy of the resulting solution was checked by grid refinement and comparison of the resulting solution with the original solution on the coarser grid. The process was repeated until an accurate solution was obtained. Based on the initial results from the coarse grid, the grid was locally refined in those regions exhibiting steep gradients of the solution variables such as the inlet, the shear layers around the inflow plume, the ceiling, and the outlet. First, a vertical column including the inlet and three cells on each side of it was refined once (by halving the mesh dimensions in each coordinate direction), and another volume around the outlet, extending three cells on each side of it and four cells below it was refined (again, by halving the mesh dimensions in each coordinate direction). Finally, a volume covering the entire ceiling area and extending four cells below, it was similarly refined. The resulting grid was again used to determine the general features of the flow. Based on the results of the initial calculations on this grid, it was determined that extra refinement of the grid in the vicinity of the inlet was required to maintain adequate accuracy. Two additional steps of refinement were done. The first involved refinement of the volume covering the inlet area and four cells away from it on all sides, and extending 18 cells above the inlet. The second refinement covered the area of the inlet and two cells away from it on all sides, and extended nine cells above the inlet. The resulting grid, referred to here as the *baseline grid*, is shown in Figs. 2(*a*) and 2(*b*) where (a) shows a side view of the vertical plane passing through the center of the inlet and (b) shows a top view of the floor and the inlet area. The baseline grid calculations were performed on a Linux cluster using ten processors. The wall-clock time per time step was about 10 s corresponding to 800 s of (wall-clock) compute time per physical second (since the time step on this grid is $\Delta t=0.0125$ s). It was found that the wall-clock time for calculations with the dynamic subgrid-scale model is nearly the same as that for the constant coefficient Smagorinsky model. To test grid convergence, one case (13% inlet turbulence intensity) was solved on *a refined grid* that contained twice the number of grid cells in each direction. The time step used on the refined grid was $\Delta t=0.006\,25$ s, so the solution for a fixed time interval was approximately 16 times more computationally expensive than the solution on the baseline grid. The computations on the refined grid were performed on a newer Linux cluster utilizing Infiniband as an interconnect, which was found to significantly decrease the wall-clock time. Using 20 cores on five nodes (each having two dual core processors) reduced the wall-clock time to about 1 s per time step.

3.3 Simulation of Inlet Turbulence. Simulation of inlet turbulence for fully developed turbulent flows can, in principle, be achieved by adding small perturbations to a laminar flow and by having a long enough computational domain in the streamwise direction to allow the turbulence to develop. In order to reduce the development region, a more viable approach is to introduce an upstream domain and to solve for the flow assuming periodicity in the streamwise direction [36]. The result of this calculation is then used as an inflow boundary condition for the main simulation.

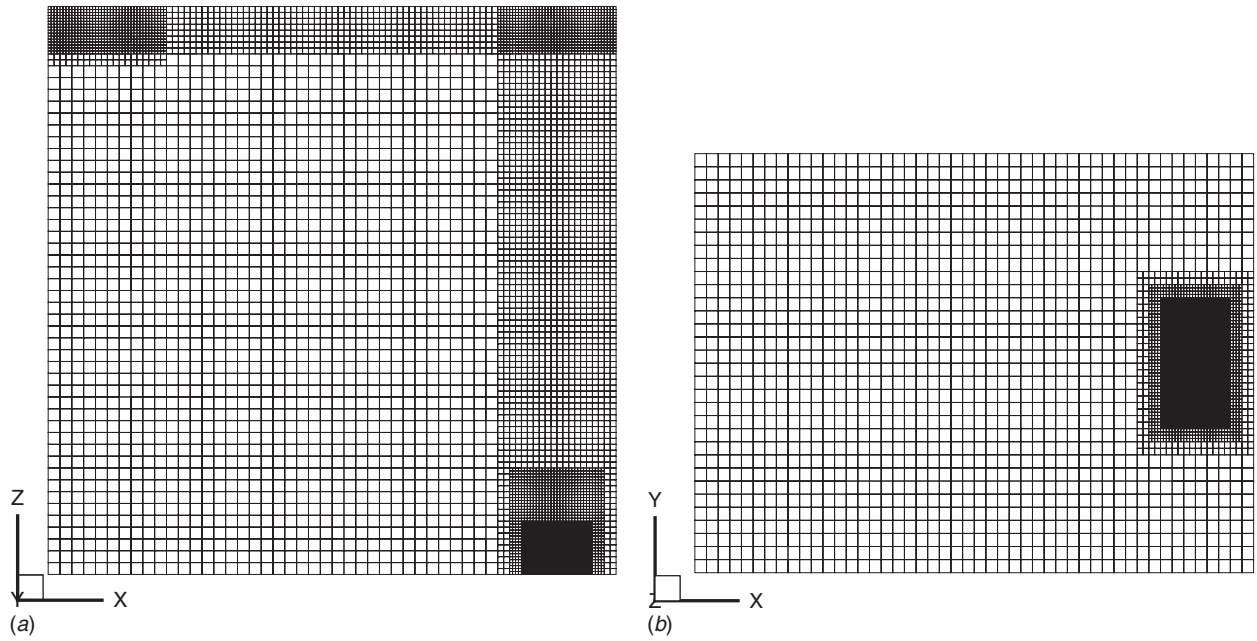

Fig. 2 Computational grid for the Indoor Flowfield Laboratory Chamber: (*a*) side (*x-z* plane) and (*b*) top (*x-y* plane) views of the baseline grid

This approach, while accurate, is too expensive to be used in engineering applications. A more practical approach is to superimpose random noise perturbations on mean velocity profiles obtained from a separate RANS simulations [37]. This approach can lead to stability problems due to the unphysical randomness of the perturbations that depend on the time step [38]. A similar approach is to use random perturbations to generate inlet turbulence with predefined characteristics. Using this technique, Lee et al. [39] built a realistic turbulence spectrum using Fourier modes with random phase shifts. This method can, however, result in an artificial transition region between the prescribed turbulent field and the solution of NS equations inside the domain [40]. FLUENT supports two techniques for generating time-dependent inlet conditions for LES. The first technique is the random flow generation (RFG) technique developed by Smirnov et al. [40]. This technique generates a divergence-free, inhomogeneous, and anisotropic flow field with predefined correlation coefficients. This method requires the specification of the anisotropic velocity correlation tensor, length, and time scales of the turbulence that may be obtained from a RANS simulation or high-resolution experimental data. The spatial and temporal variations of the resulting velocity field follow a Gaussian spectrum with the specified length and time scales. Smirnov et al. [40] successfully applied this technique to the simulation of ship wakes. The ship hull part of the domain was simulated using a RANS calculation. The resulting anisotropic field was then used as an inflow plane to the wake part of the domain, which was simulated with LES. The length and time scales required by the RFG were deduced from the length scales predicted by the RANS. The RFG is a more realistic representation of the turbulence than a simple Gaussian distribution of velocity as it guarantees that the resulting velocity field satisfies the continuity and anisotropy constraints. The RFG, however, does not guarantee that the resulting field satisfies the momentum equations and is thus an approximate method [40]. The second technique for inlet turbulence generation in FLUENT is the vortex method developed by Mathey et al. [41]. With this approach, a perturbation is added to the specified mean velocity profile via a fluctuating vorticity field (two-dimensional in the plane normal to the mean-flow direction). The use of this method requires the specification of the mean turbulent kinetic energy and dissipation rate profiles at the inlet of the computational domain [30]. The accuracy of this method has been investigated using several test cases [38] such as turbulent channel and pipe flows and the flow over periodic hills. The flow over periodic hills represents a case where the dynamics of the flow are controlled to a great extent by the level of upstream turbulence. Mathey et al. [41] compared two approaches for specifying the inlet turbulence with a reference simulation in which periodic boundary conditions were used. In the first test simulation, the vortex method was used to generate the inlet boundary conditions and in the second test simulation random noise was used. They found that the random noise simulation overestimated the re-attachment length by 50% and underestimated the spreading rate of the shear layer. They also found that the random noise underestimated the turbulence level inside the shear layers by one order of magnitude. They explained these results by the low level of kinetic energy in the random noise simulation due to the damping of the nonphysical random fluctuations at the inlet. This demonstrated the importance of the upstream history of the turbulence on the subsequent production mechanisms and thus the sensitivity of the turbulence to the accuracy of the inlet boundary conditions [38]. We therefore selected FLUENT's built-in vortex method to generate the time-dependent inlet conditions.

4 Results and Discussion

We begin by showing a comparison of solutions on the refined and the baseline grids to demonstrate that the solution on the baseline grid is spatially converged. On this basis, the baseline grid is used for all the subsequent computations. The effect of the turbulence level at the inlet is studied assuming a uniform mean velocity profile and three levels of isotropic turbulence at the inlet. Then, the 13% inlet turbulence case with uniform mean profiles is compared with the case using the measured inlet velocities and turbulence intensities to determine the significance of the detailed profiles at the inlet. We also compare the performance of different modeling approaches: the constant coefficient Smagorinsky subgrid-scale model and the dynamic model for the 13% case with uniform inlet profiles, and the constant coefficient model with the k-ϵ model at 0% and 13% inlet turbulence intensity.

4.1 Grid Convergence Study. The grid resolution for LES should be sufficient to resolve the bulk of the turbulent kinetic

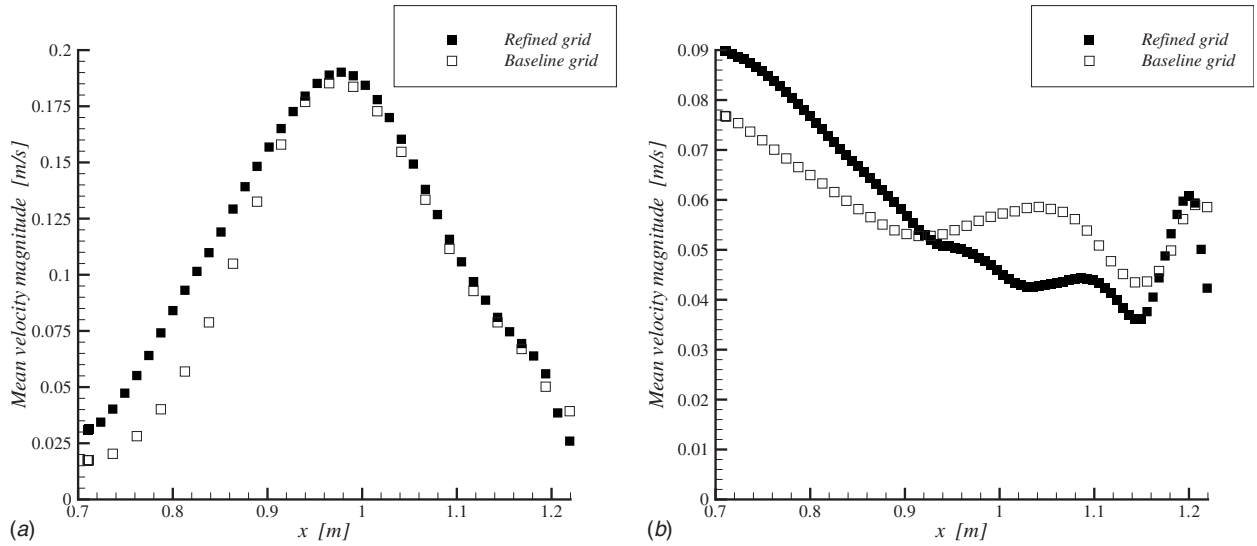

Fig. 3 Comparison of mean velocity magnitude on the baseline and the refined grids at (a) $z/L=-0.2$ and (b) $z/L=0.9375$

energy. If this is achieved, LES should be at most weakly dependent on the particular subgrid-scale model used in the computations. In FLUENT, the mixing length for the subgrid scales L_s and the subgrid-scale eddy viscosity $\nu_t=\mu_t/\rho$ are used to construct an estimate for the subgrid-scale turbulent kinetic energy k_s defined as

$$k_s=\frac{\nu_t^2}{L_s^2} \tag{16}$$

which is referred to by FLUENT as the "subtest kinetic energy." Figures 3 and 4 compare the mean and root mean square (rms) of the velocity magnitude obtained from the solutions on the baseline and the refined grids. It is seen that the shapes of the profiles agree reasonably well and that the deviations are generally small, reaching a maximum of about 30%. It is also seen that the deviations at the stations closest to the inlet (Fig. 3(*a*) and 4(*a*) at $z/L=-0.2$) occur predominantly in the shear layers. Figure 5 also compares the turbulent kinetic energy obtained from the solutions on the two grids including the subgrid-scale contributions. It is clear that on the refined grid the subtest kinetic energy is less than 5% of the total turbulent kinetic energy, except very near the inlet, so the solution on this grid is judged to be well resolved. The subtest kinetic energy on the baseline grid is somewhat larger, but still small enough relative to the total turbulent kinetic energy that we judge the solution on the baseline grid to be adequately resolved for the subsequent computations. This conclusion is supported by the earlier comparison of the mean and rms profiles shown in Figs. 3 and 4.

4.2 Effect of Inlet Turbulence Level Using Plug-Flow Inlet Conditions. Figures 6(*a*) and 6(*b*) show the contour plots of the instantaneous and mean velocity magnitudes, respectively, along the vertical *x-z* plane passing through the middle of the inlet for the 0% inlet turbulence intensity case. It is clear that the jet in this case is very confined and that there is little mixing with the room air. The jet flows straight up toward the ceiling, bends 90 deg, and flows along the ceiling until it reaches the exit. Other than this basic flow pattern, there are no significant organized motions or

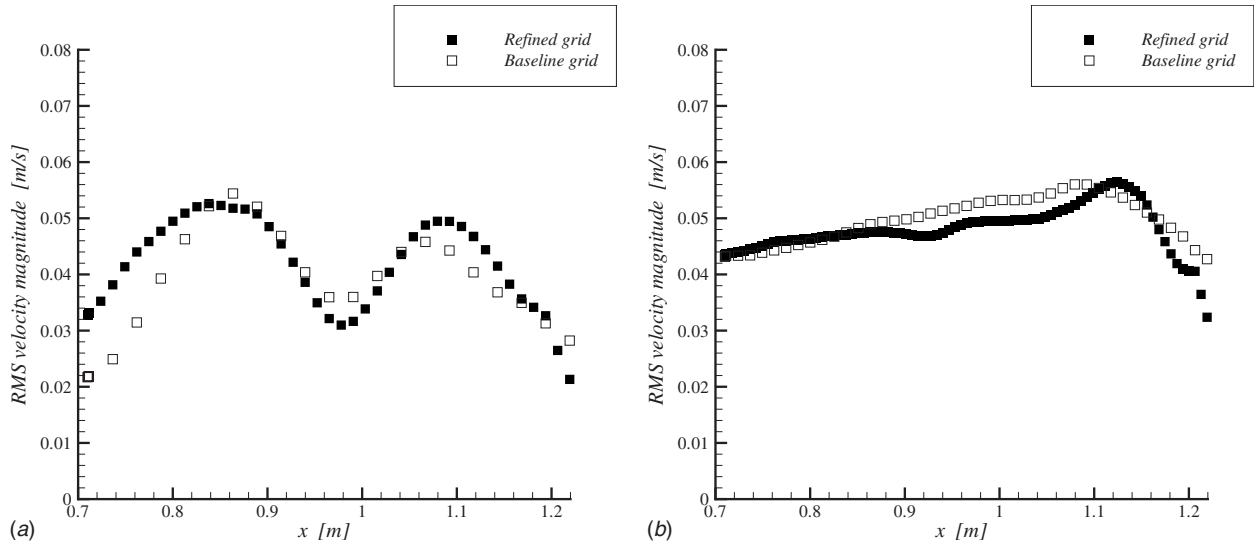

Fig. 4 Comparison of the rms of the velocity magnitude on the baseline and the refined grids at (a) $z/L=-0.2$ and (b) $z/L=0.9375$

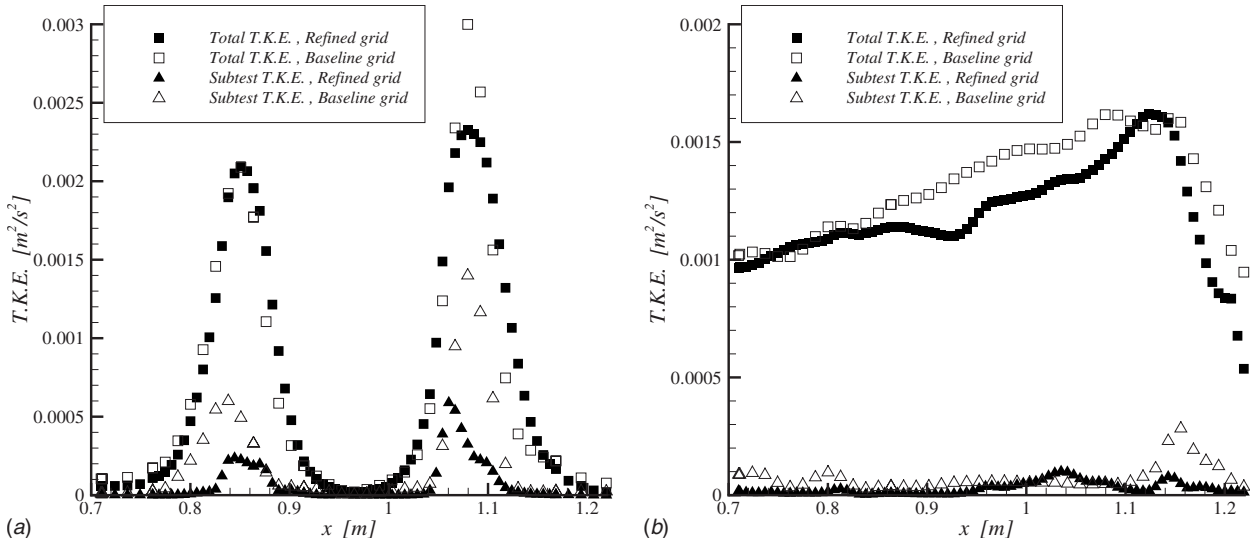

Fig. 5 Comparison of turbulent kinetic energy on the baseline and the refined grids at (*a*) $z/L=-0.8$ and (*b*) $z/L=0.9375$

circulation patterns in the room. The figures for the instantaneous and mean velocities are also reasonably similar, especially near the inlet, suggesting that the levels of turbulence are quite low. Near the ceiling, however, the jet has spread enough to interact with the front wall, generating turbulence there and in the ceiling's boundary layer. A complicated unsteady flow pattern, dominated by eddying motions, is observed in the ceiling's stagnation layer.

Figures 7 and 8 show the corresponding contour plots for the cases of 5% and 13% inlet turbulence intensity. It is seen in both cases that the jet spreads and mixes with the room air more rapidly and starting closer to the inlet than in the laminar inflow case. The mean flow, however, is still generally confined to a vertical column around the inlet and a horizontal slab along the ceiling, with only weak circulation elsewhere in the room. The reason for the more rapid mixing and spreading of the jet, and the increased levels of turbulence relative to the laminar inflow case is that the inlet jet, seeded with turbulence, undergoes a more rapid transition to a turbulent jet than the laminar inflow case. Figures 7 and 8 show significant similarity between the 5% and 13% turbulence intensity cases in both the mean and the instantaneous flow velocity magnitudes. It is also noted that the instantaneous contours in both cases are characterized by the intermittent breaking-off of blobs of high velocity fluid from the jet core that increase the local levels of turbulence as they sweep through the domain.

The above observations can be seen more quantitatively by looking at profiles of the mean velocity magnitude and the rms of the velocity fluctuations for the different levels of the inlet turbulence intensity. Figures 9 and 10 compare the profiles of the mean velocity magnitude at stations located at $z/L=-0.4$, $z/L=0.0$, and $z/L=0.75$, plotted along the horizontal lines extending from $x=0.71$ m all the way to the front wall, along the center of the inlet ($y=0$). As can be seen, the mean velocity profiles in the 5% and 13% cases are quite similar, exhibiting nearly the same spreading rate. This is consistent with the notion that, beyond a threshold level of the inlet turbulence intensity, the subsequent development of the jet is only weakly dependent on the inlet conditions. It is also noted that the profiles of the 5% and 13% cases exhibit significant asymmetry due to the front wall. The laminar inflow case, in contrast, has nearly symmetric profiles up until $z/L=0.75$, where the jet has spread enough to interact with the wall, causing an asymmetry of the profile to develop.

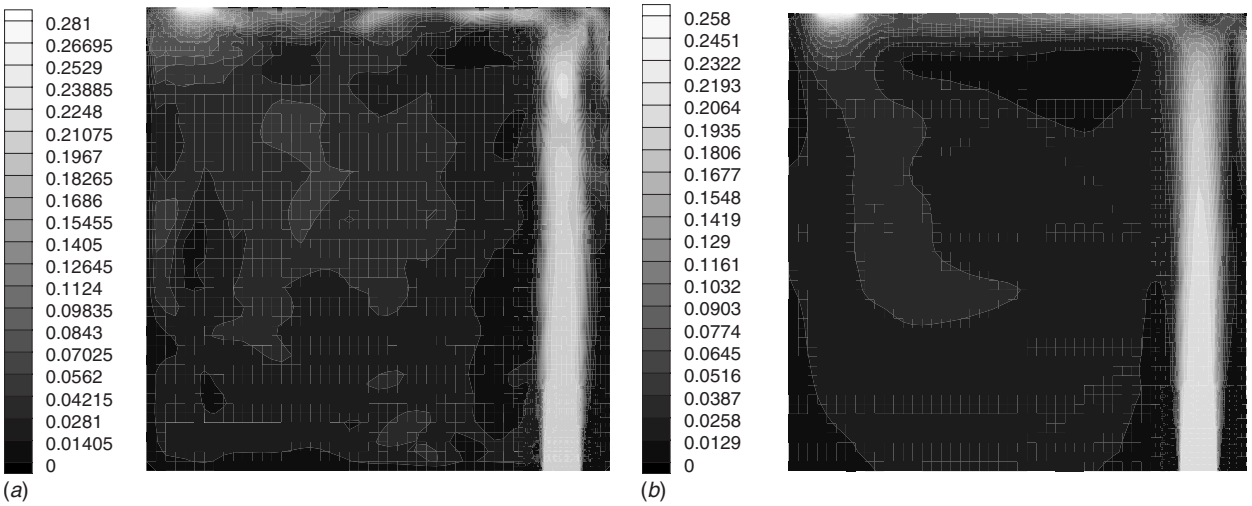

Fig. 6 (*a*) Instantaneous and (*b*) mean velocity contours on center plane; 0% inlet turbulence (units are in m/s)

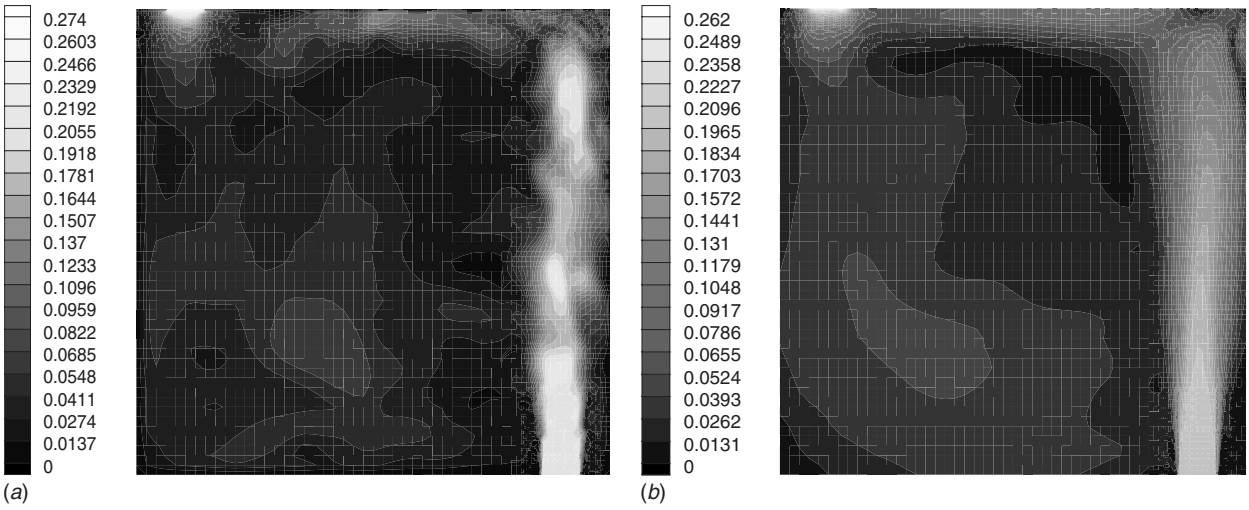

Fig. 7 (*a*) Instantaneous and (*b*) mean velocity contours on center plane; 5% inlet turbulence (units are in m/s)

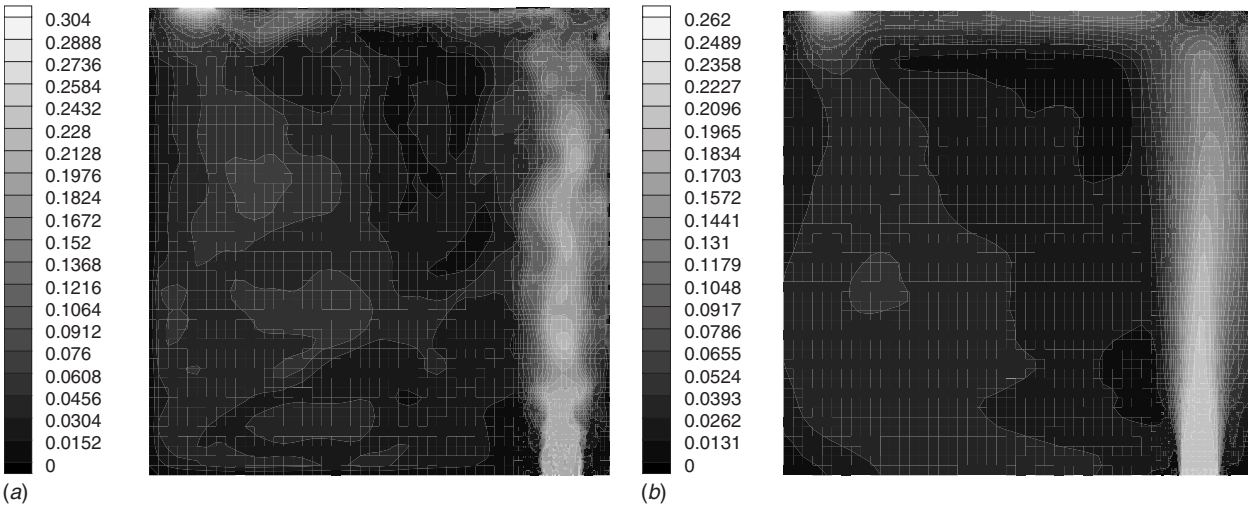

Fig. 8 (*a*) Instantaneous and (*b*) mean velocity contours on center plane; 13% inlet turbulence (units are in m/s)

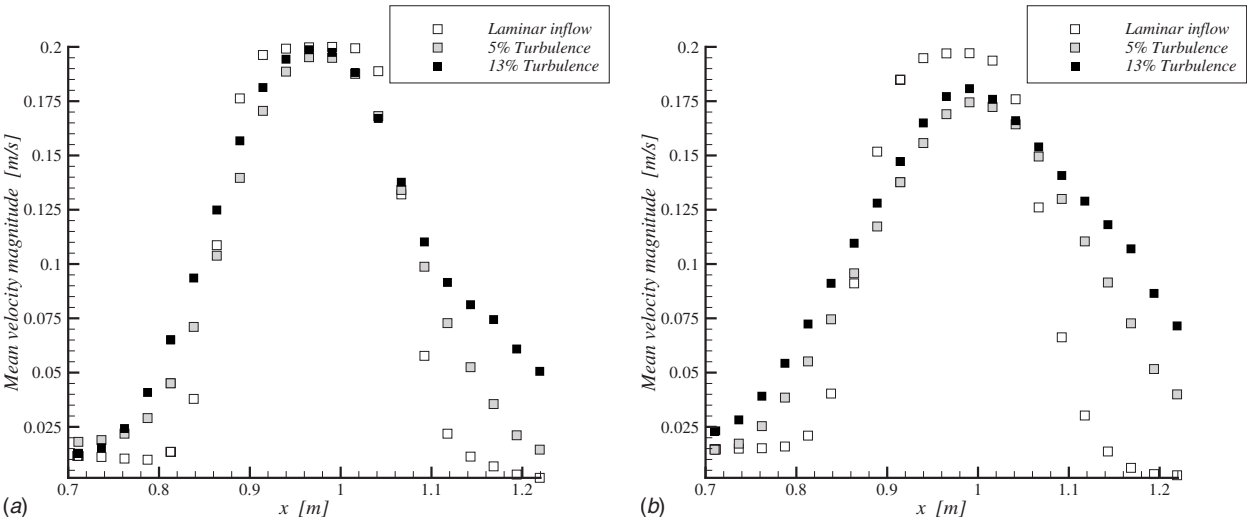

Fig. 9 Comparison of the mean velocity magnitude for three levels of inlet turbulence intensity at (*a*) $z/L=-0.4$ and (*b*) $z/L=0.0$; baseline grid

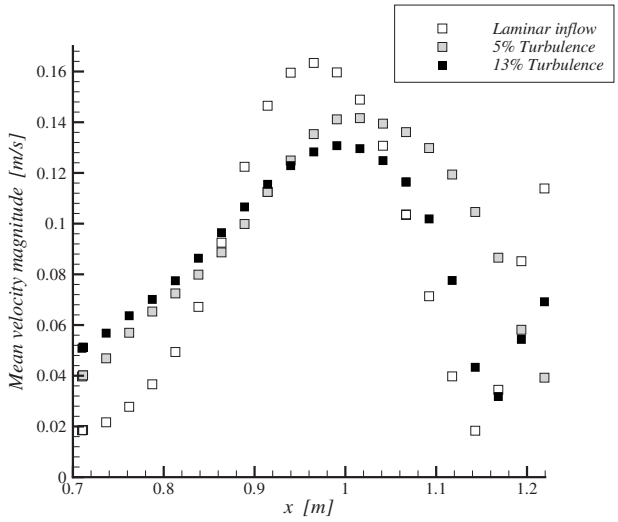

Fig. 10 Comparison of the mean velocity magnitude for three levels of inlet turbulence intensity at $z/L=0.75$; baseline grid

Profiles of the velocity rms are shown in Figs. 11 and 12. Once again the 5% and 13% cases show quite similar profiles throughout the computational domain. The behavior of the laminar inflow case needs some elaboration. At the $z/L=-0.4$ and $z/L=0.0$ stations, the level of turbulence is significantly less than for the 5% and 13% cases because of the laminar state of the entering jet. However, near the ceiling, the shear layers have grown enough to begin to interact with the front wall and turbulence is generated there and also in the ceiling's boundary layer. The contours in Fig. 6 show the generation of a blob of high velocity fluid near the ceiling, which can contribute to the high levels of turbulence near the ceiling. Accordingly, the rms levels of the velocity fluctuations in the laminar inflow case are seen to be higher than the rms levels for the 5% and 13% cases near the ceiling (see Figs. 11 and 12).

The significant differences between the simulation results for the 0% and both the 5% and 13% cases cannot be captured by the standard k-ϵ model, which is designed primarily for fully developed turbulent flows. This very fact led Loomans [42], who investigated the effect of inlet turbulence intensity level on the flow field of a displacement ventilation system in a full-scale room using the standard k-ϵ model, to conclude that the level of inlet

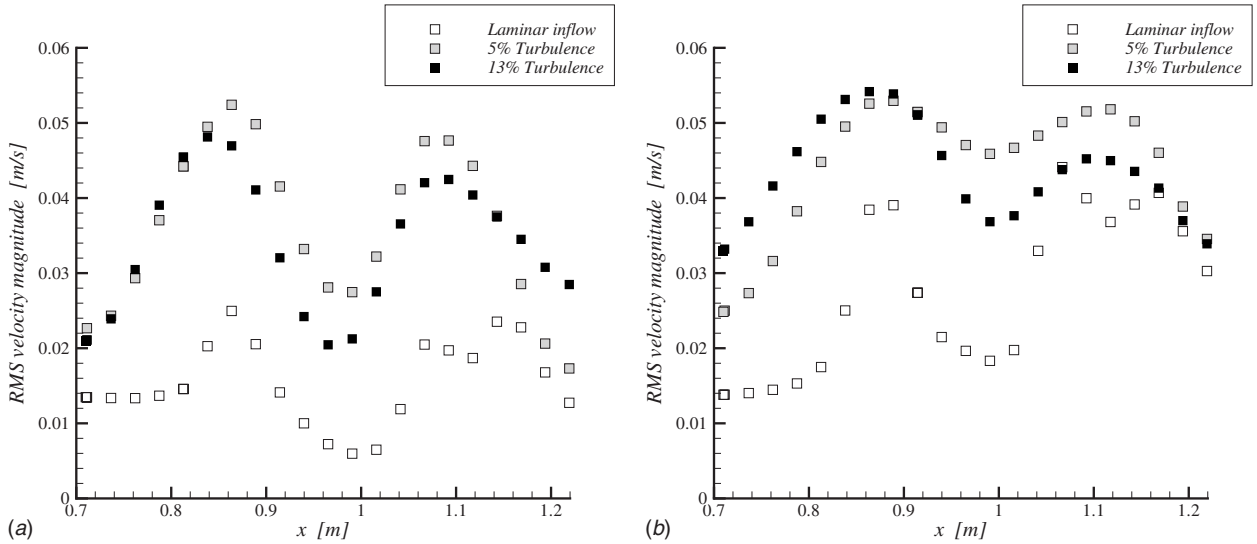

Fig. 11 Comparison of the rms velocity magnitude for three levels of inlet turbulence intensity at (*a*) $z/L=-0.4$ and (*b*) $z/L=0.0$; baseline grid

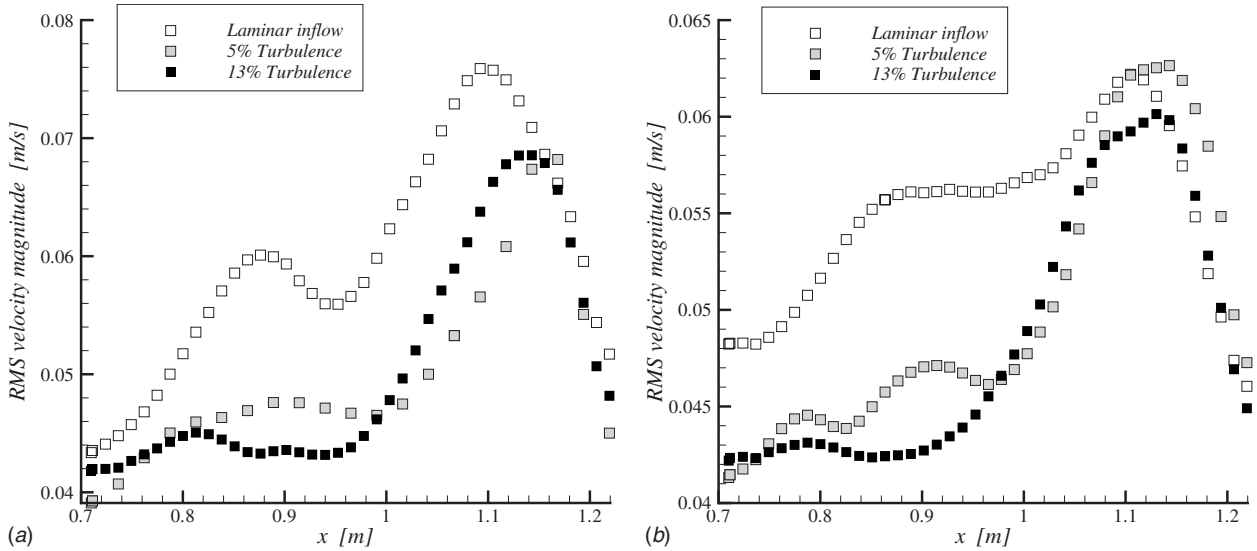

Fig. 12 Comparison of the rms velocity magnitude for three levels of inlet turbulence intensity at (*a*) $z/L=0.875$ and (*b*) $z/L=0.9375$; baseline grid

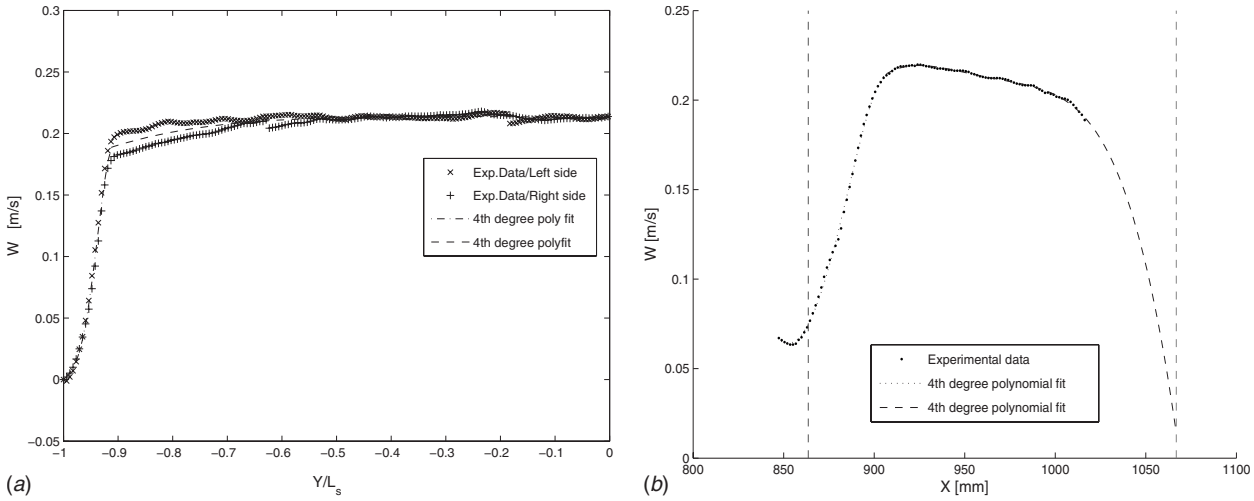

Fig. 13 Experimental data and curve fits along the (*a*) long and (*b*) short sides of the inlet. In (*a*), L_s is the half-length of the inlet section.

turbulence has a negligible effect on the flow field especially far from the inlet. As we will demonstrate, the standard k-ϵ model is insensitive to the level of inlet turbulence intensity and accordingly cannot be used to accurately predict the flow behavior for situations wherein the flow is most probably transitional in nature. It is also noted that the levels of inlet turbulence intensities investigated by Loomans were 10% and 35% and accordingly the flow was most probably fully developed even for the lower value. Using the k-ϵ model for the simulation of a jet in a two-dimensional cavity with inlet turbulence intensities of 4–37.4%, Joubert et al. [43] also concluded that the effect of the inlet turbulence intensity on the flow field was negligible.

The LES results for the 5% and 13% cases are consistent with the study of Jiang [44] who used LES and the standard k-ϵ model to investigate the effects of inlet boundary conditions on the flow field in a full-scale room. At the highest studied ventilation rate of 19.5 air change per hour (ACH), corresponding to an inlet mean velocity of 1.43 m/s and a Reynolds number of 4895, Jiang investigated three cases: (1) uniform inlet velocity profile and uniform turbulence intensity of 10%, (2) profiled velocity and turbulent kinetic energy from hot wire measurements, and (3) experimental velocity profile and uniform inlet turbulence intensity of 10%. In LES, the turbulence at the inlet was generated using a random number generator technique. The author concluded that the effect of inlet conditions on the flow field is confined to the vicinity of the inlet and negligible elsewhere in the flow field. Although the average level of inlet turbulence intensity in case (2) could not be inferred, the high ventilation rate/Reynolds number used in this study indicate that the flow was fully developed in nature. Our LES simulation with laminar inflow conditions shed some light on the potentially significant differences between simulations at low levels of inlet turbulence and those with high enough levels of inlet turbulence to cause the flow to rapidly reach a fully developed state. The existence of a threshold inlet turbulence level, above which the flow becomes independent of the inlet turbulence level, is a hypothesis that requires further investigation.

4.3 Effects of Realistic Inlet Flow Conditions. Here we consider the importance of the detailed mean and turbulence profiles at the inlet on the flow inside the room. We replace the idealized inlet velocity profile used in Sec. 4.2 by the experimentally measured inlet conditions. The first stage of utilizing the PIV experimental data obtained at Syracuse University [45] in our simulations involved interpretation of the data, which contained artifacts from the measurement technique and experimental noise. In addition, data could not be obtained for that part of the inlet closest to the front wall, due to distortions and reflections from the glass wall; consequently, assumptions had to be made about the profiles of the measured quantities. The experimental data consist of the mean values of the three components of velocity and the rms of their fluctuations. The mean velocity components in the plane of the inlet, i.e., the U and V components, were deemed small enough to neglect, whereas the vertical component W of the velocity was fitted to a smooth polynomial. The variations parallel to the long side of the inlet were not as significant as those across the short side, and a fit of the averaged experimental data on both sides was used. Figure 13(*a*) shows two fourth-order polynomials (one covering most of the profile and one representing the shear layer portion). In the direction of the short side, the interpretation of the data was complicated by the fact that part of the inlet was not covered by the measurement window; hence this part of the data was missing. We extrapolated the missing data using two, fourth-order, polynomials that represent the profile, including the missing segment, as shown in Fig. 13(*b*). The turbulent kinetic energy and the root mean square of the fluctuating velocities were assumed symmetric across the short side of the duct, with negligible variation in the direction of the long side, as shown in Fig. 14 (which shows only half of the profile since it is assumed symmetric).

FLUENT calculations with these fitted inlet profiles were run and compared with the 13% case with uniform profiles. Figures 15 and 16 show comparisons of the mean velocity at four vertical stations. Note that the significant differences at the lowest station ($z/L=-0.8$) become weaker with increasing distance from the inlet. The maximum deviation between the two cases occurs in the shear layers, where the deviation of the measured inlet turbulent kinetic energy from the spatially averaged value is greatest. This suggests that there is some memory of the inlet conditions throughout the flow.

Similar behavior of the rms of the velocity is shown in Figs. 17 and 18, where close to the inlet (at the $z/L=-0.8$ and $z/L=-0.4$ stations) the profiles are significantly different, whereas close to the ceiling, the two cases predict similar levels of turbulence (notice the offset of the origin of the vertical axis in Fig. 18 amplifies the small differences between the profiles). So in general the flow field exhibits sensitivity to the inlet flow conditions primarily near the inlet. As the flow evolves spatially, the effect of the inlet conditions becomes less pronounced. This conclusion is in agreement with Jiang's [44] conclusions from his LES and k-ϵ model calculations for similar comparisons. Joubert et al. [43] also reported that using a parabolic inlet velocity profile as opposed to a

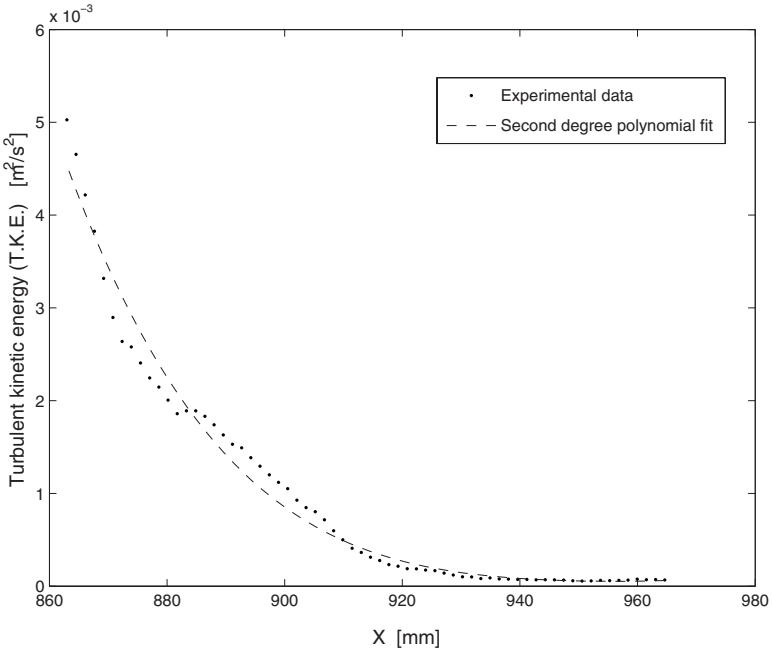

Fig. 14 Fitted profile of the turbulent kinetic energy

uniform profile does not affect the mean velocity in the two-dimensional cavity flow that they analyzed with the k-ϵ model; however, they found significant differences in the predicted levels of turbulence in the cavity, which they explained on the basis of the contribution of the shearing already present in the inflow in the parabolic profile case. It should be noted that the wall jet studied in their two-dimensional simulation is fundamentally different from the present configuration. The close proximity of the jet to the top boundary may have caused the greater sensitivity. They also noted that the width of the slot has an important effect on the turbulence level within the cavity.

4.4 Comparison of the Constant Coefficient and Dynamic Smagorinsky LES Models. The success of a subgrid-scale model can be characterized by how well it predicts the large-scale statistics of a given turbulent flow. It is to be expected that the results should be relatively insensitive to the subgrid-scale model if the large-scale, energy-containing, turbulent motions are sufficiently resolved. The dynamic model adjusts the coefficient C_s locally in space and time based on the resolved scales. In this way, the model responds to changes in the large-scale turbulent motions, and thus it tends to be self-correcting in the sense that it adjusts the eddy viscosity coefficient based on the energy in the resolved scales. In this section, a comparison is made between the results obtained with the constant coefficient Smagorinsky subgrid-scale model and the dynamic model for the case of 13% inlet turbulence intensity, with uniform mean inlet profiles. Figures 19–22 compare the mean and the rms of the velocity magnitudes obtained from the constant coefficient and the dynamic model in both the

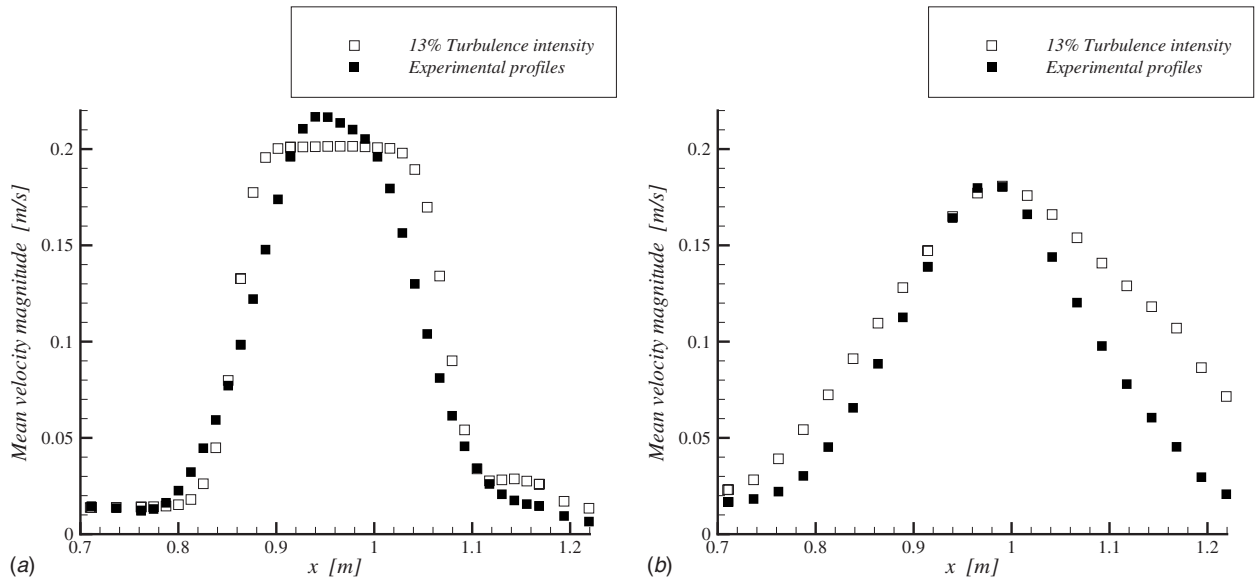

Fig. 15 Mean velocity magnitude at (*a*) $z/L=-0.8$ and (*b*) $z/L=0.0$; comparison of results with plug flow and experimentally determined inlet conditions

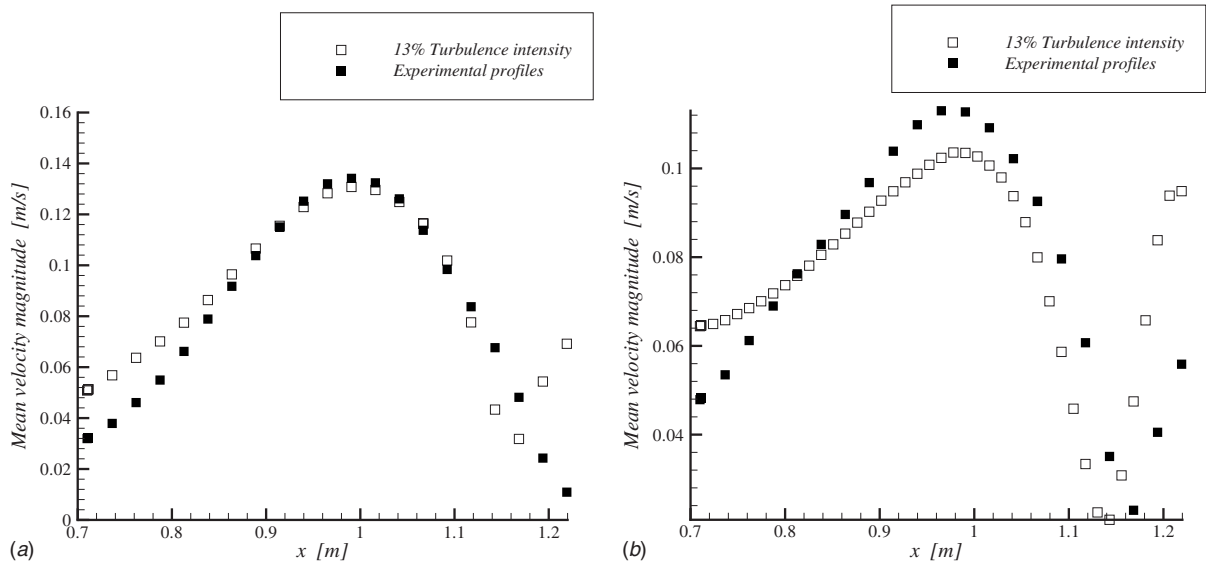

Fig. 16 Mean velocity magnitude at (*a*) $z/L=0.75$ and (*b*) $z/L=0.875$; comparison of results with plug flow and experimentally determined inlet conditions

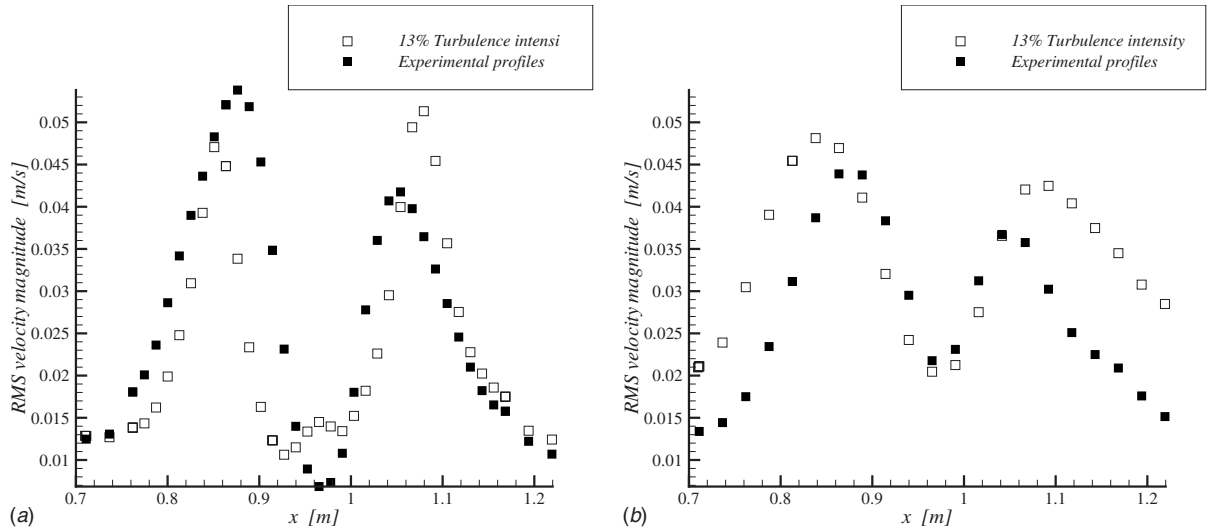

Fig. 17 rms velocity magnitude at (*a*) $z/L=-0.8$ and (*b*) $z/L=-0.4$; comparison of results with plug flow and experimentally determined inlet conditions.

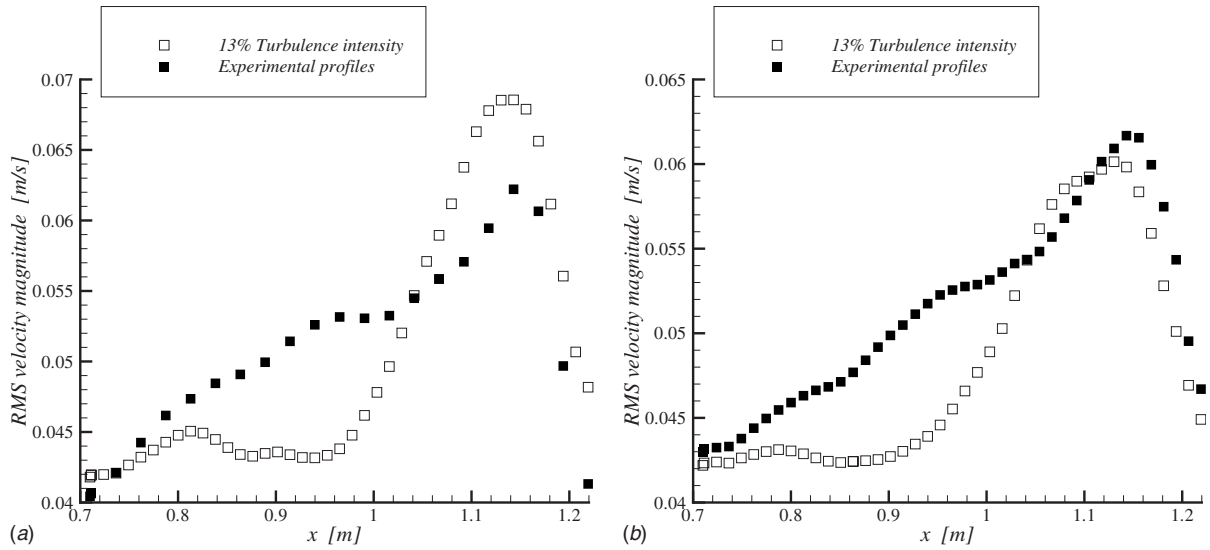

Fig. 18 rms velocity magnitude at (*a*) $z/L=0.875$ and (*b*) $z/L=0.9375$; comparison of results with plug flow and experimentally determined inlet conditions

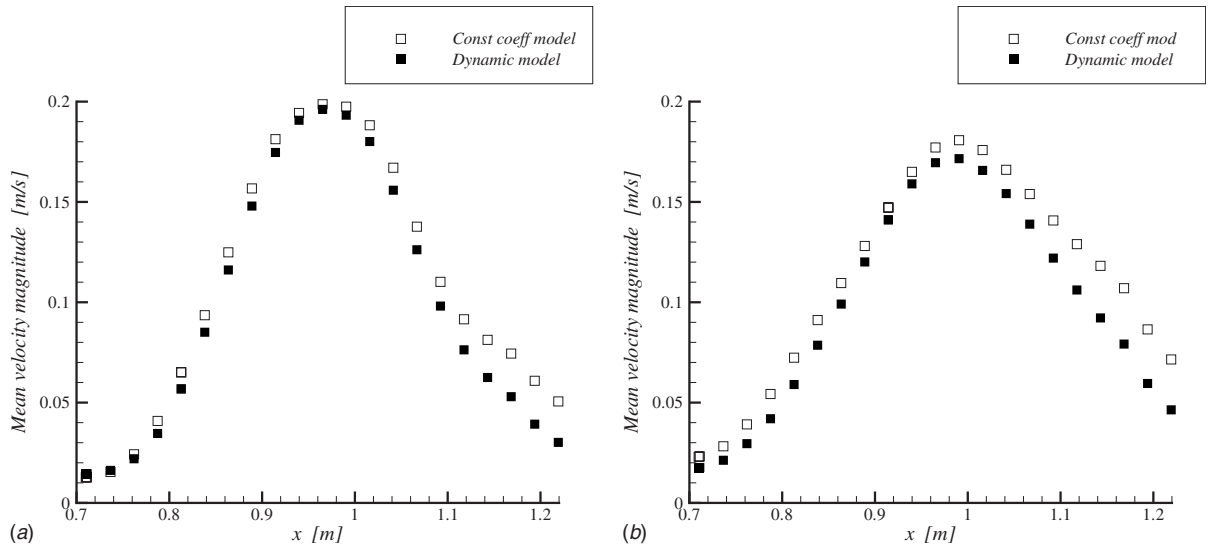

Fig. 19 Mean velocity magnitude at (*a*) $z/L=-0.4$ and (*b*) $z/L=0.0$; comparison of results using constant-coefficient and dynamic Smagorinsky models

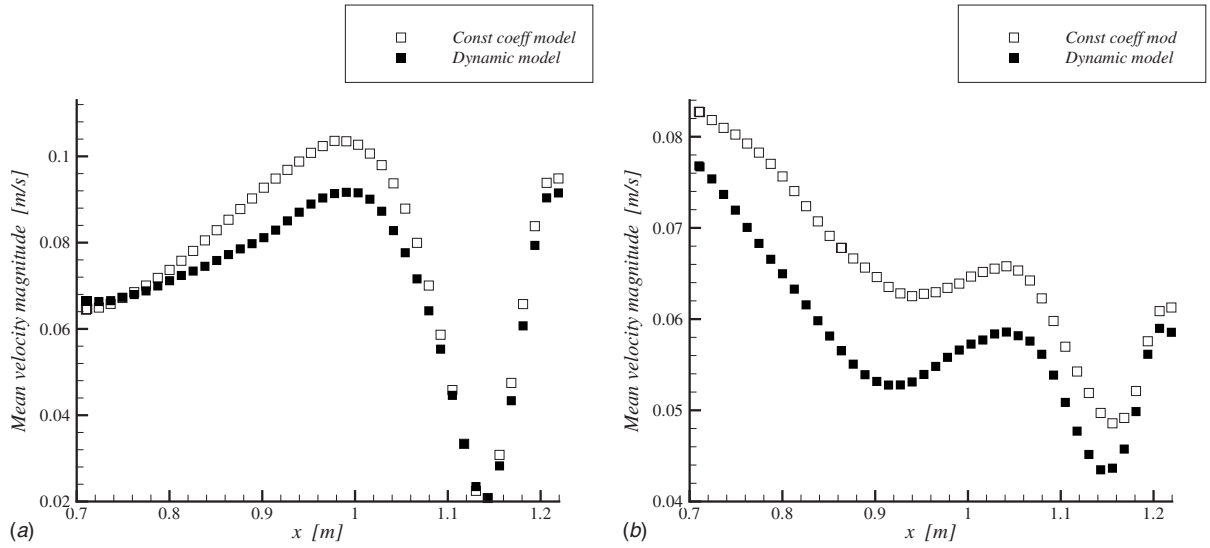

Fig. 20 Mean velocity magnitude at (*a*) $z/L=0.875$ and (*b*) $z/L=0.9375$; comparison of results using constant-coefficient and dynamic Smagorinsky models

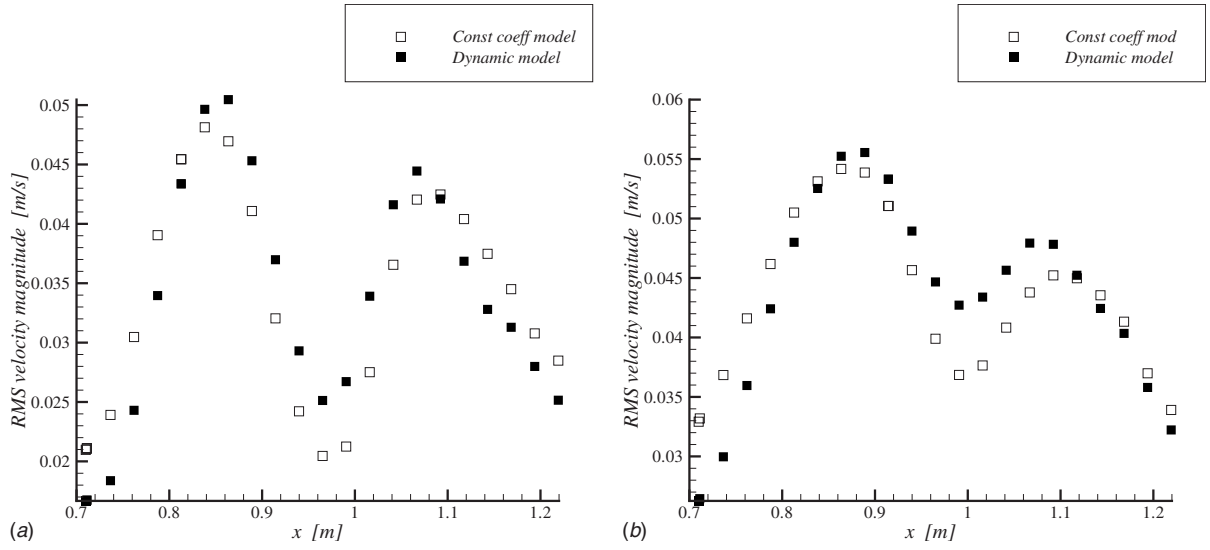

Fig. 21 rms velocity magnitude at (*a*) $z/L=-0.4$ and (*b*) $z/L=0.0$; comparison of results using constant-coefficient and dynamic Smagorinsky models

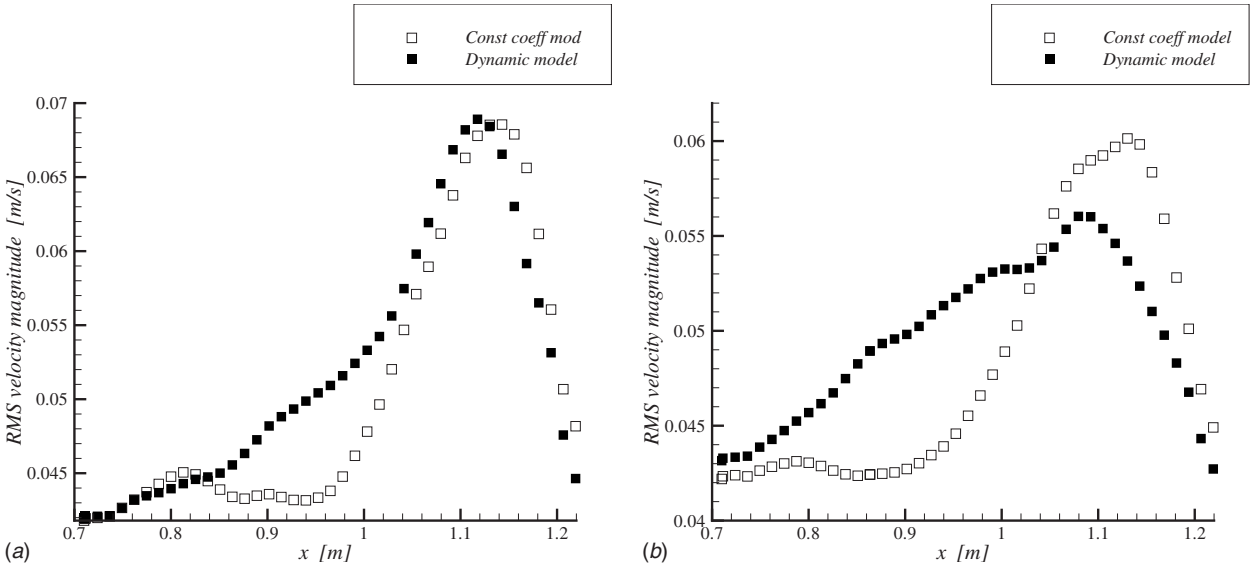

Fig. 22 rms velocity magnitude at (*a*) $z/L=0.875$ and (*b*) $z/L=0.9375$; comparison of results using constant-coefficient and dynamic Smagorinsky models

near- and the far-field of the jet. Maximum deviations of about 20–30% in the mean velocity magnitude occur near the inlet (where the largest dissipation rates are concentrated), at the $z/L=-0.4$ and $z/L=0.0$ stations (notice the origin offset in the plots near the ceiling, Figs. 20 and 22). Further from the inlet, as the jet loses its strength, maximum deviations of about 10–15% are seen at the $z/L=0.875$ and $z/L=0.9375$ stations (see Figs. 19 and 20). Similar behavior of the rms of the velocity magnitude is observed in Figs. 21 and 22, where at the $z/L=-0.4$ and $z/L=0.0$ stations, the maximum deviations are about 20%, whereas at the $z/L=0.875$ and $z/L=0.9375$ stations, the deviations are about 10–15%. The differences described above are expected, as it was shown that the subgrid-scale contribution to the total turbulent kinetic energy is largest near the inlet and smallest near the ceiling (see Fig. 5(*a*) and 5(*b*)). These results demonstrate that the constant coefficient model agrees reasonably well with the dynamic model, at least for the low-order statistics of the flow. This weak dependence on the subgrid-scale model reflects the fact that the large energy-containing scales of motion are well resolved.

4.5 k-ϵ Model Predictions at Low Inlet Turbulence Levels. As already alluded to in Sec. 4.2, significant flow field differences can potentially exist between the LES and the standard k-ϵ model predictions when the flow is slowly developing in space or time. In this section, we have systematically studied these model differences for the two extreme levels of inlet turbulence, i.e., 0% and 13%. For the 0% inlet turbulence case, LES predicts that the flow develops slowly in space and, accordingly, the flow field is a mixed laminar and turbulent state. For the 13% case, the jet rapidly transitions to a fully developed turbulent state close to the inlet. Figures 23 and 24 compare the mean velocity magnitude and turbulent kinetic energy from two simulations using the standard k-ϵ model with 0% and 13% inlet turbulent levels, respectively. It is seen that the solution is nearly insensitive to the level

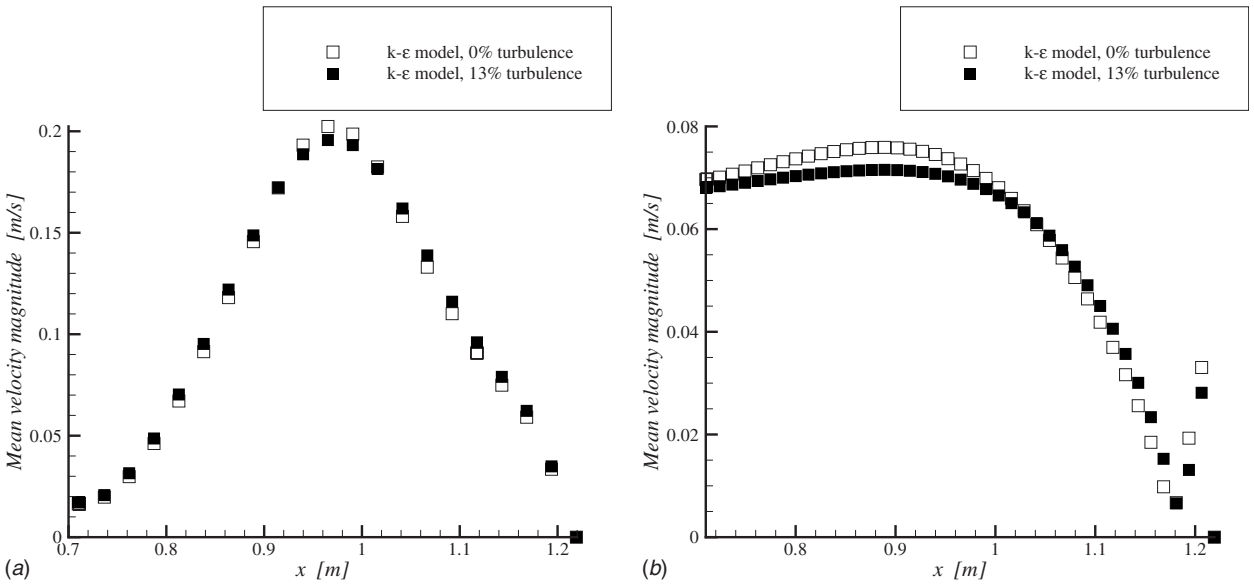

Fig. 23 Mean velocity magnitude from k-ϵ model at (*a*) $z/L=-0.6$ and (*b*) $z/L=0.875$

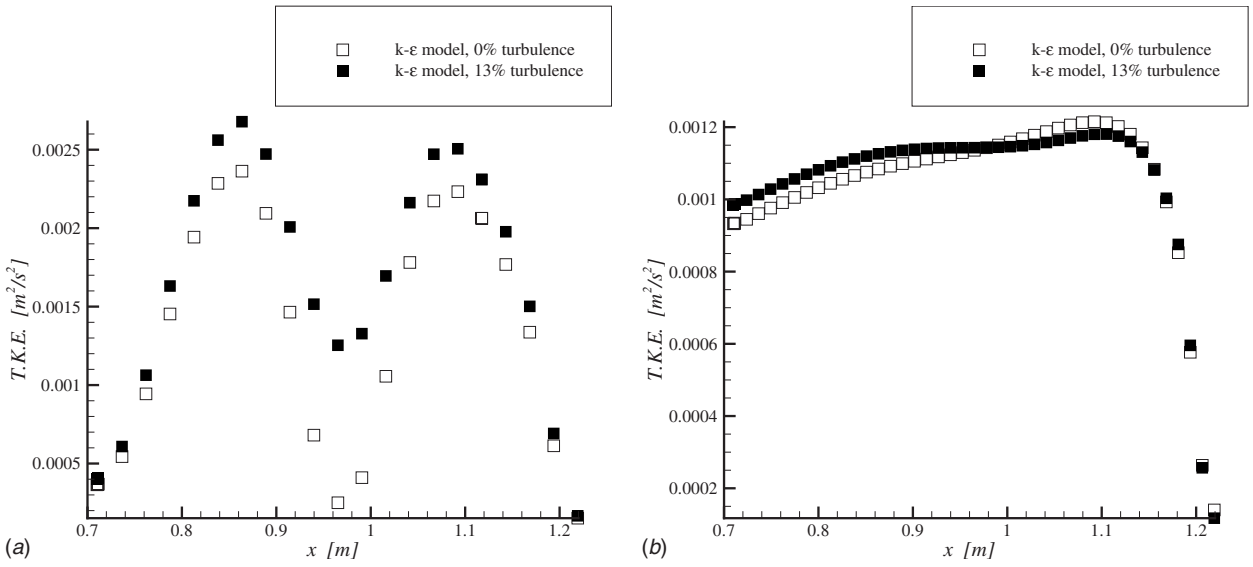

Fig. 24 Turbulent kinetic energy from k-ϵ model at (*a*) $z/L=-0.6$ and (*b*) $z/L=0.875$

of inlet turbulence especially far from the inlet. The slow development of the jet predicted by LES in the 0% case is not observed with the k-ϵ model. To emphasize this point, we compare the solution from the k-ϵ and LES, using the constant coefficient model, at 0% and 13% inlet turbulent levels. Figure 25 shows the comparison for the mean velocity magnitude profile very close to the inlet ($z/L=-0.8$) at 0% and 13% inlet turbulent intensities. At 0% turbulence intensity, LES is predicting a flat velocity profile with a sharp gradient separating the potential core from the quiescent fluid outside. The k-ϵ model, in contrast, predicts a much more diffuse profile with curved shape similar to the profile for a fully developed free jet. The two model predictions are in better agreement at the 13% turbulence intensity, as the turbulence is more nearly fully developed leading both models to predict a smoother profile. The inability of the k-ϵ model to predict the slow development of the jet at 0% inlet turbulence intensity leads to an overprediction of the spreading rate. As discussed in Ref. [2], a well-known deficiency of the k-ϵ model is that it significantly overpredicts the rate of spreading for the round jet. Although these differences could be reduced by adjusting the value of $C_{\epsilon 1}$ or $C_{\epsilon 2}$, we did not feel that this would be justified. Figure 26 shows the mean velocity profile at a location well removed from the inlet ($z/L=0.75$). The agreement between the LES and k-ϵ predictions is better at the 13% inlet turbulence intensity level. Nevertheless, it is clear that the k-ϵ model fails to capture the correct qualitative behavior near the upper right corner ($x \sim 1.22$ m), as it shows a nearly stagnant region, whereas the LES model predicts that there are small patches of intermittent activity in the corner. Figure 27 shows a comparison of the resolved turbulent kinetic energy from the LES model to the turbulent kinetic energy from the k-ϵ model at 0% and 13% inlet turbulent intensities. In the laminar inflow case, it is clear that LES is predicting the correct physical behavior of the jet close to the inlet where there is no active mechanism for turbulence generation yet at $z/L=-0.8$ as the shear layer thickness is close to zero and the jet

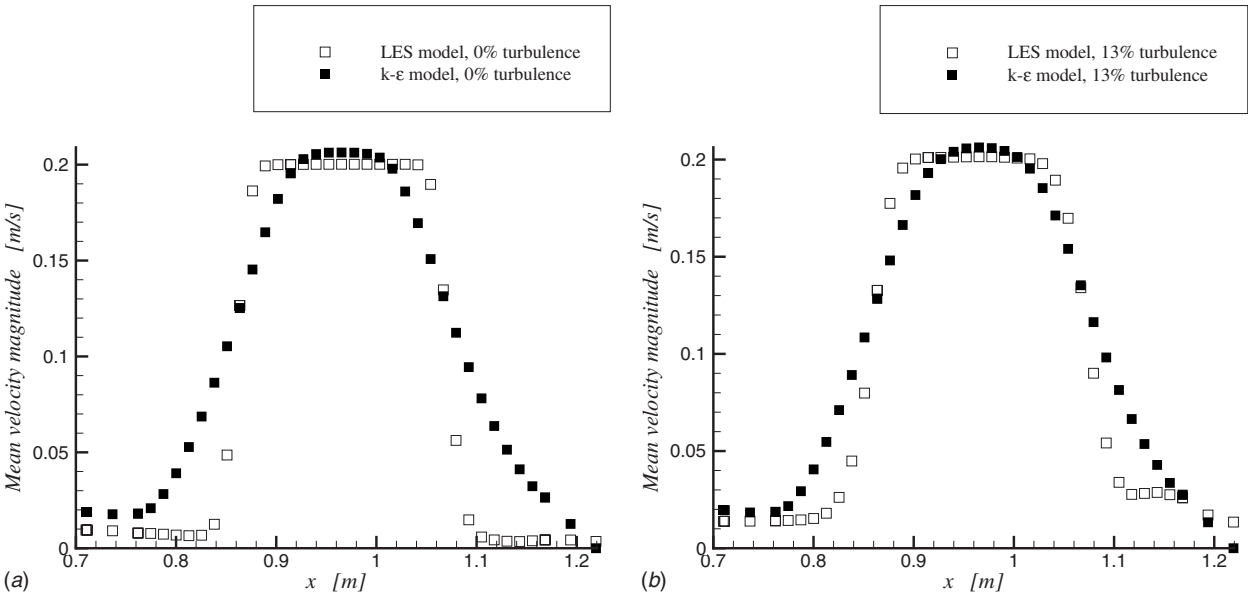

Fig. 25 Mean velocity magnitude from k-ϵ and LES models at $z/L=-0.8$: (*a*) 0% and (*b*) 13% inlet turbulence intensities

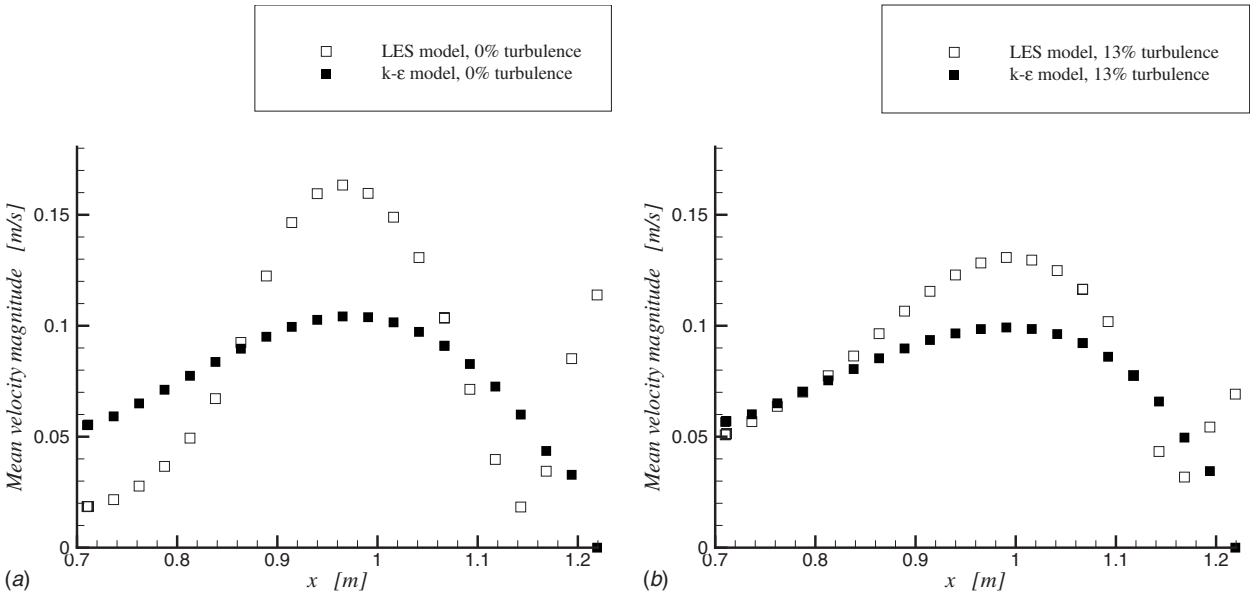

Fig. 26 Mean velocity magnitude from k-ϵ and LES models at $z/L=0.75$: (*a*) 0% and (*b*) 13% inlet turbulence intensities

inflow is laminar. The k-ϵ model on the other hand is predicting unrealistically high levels of turbulence near the inlet. In the 13% turbulence intensity case, although the k-ϵ model qualitatively captures the double-peaked profile, it still significantly overpredicts the turbulent kinetic energy relative to the LES model. Figure 28 presents similar comparisons at a location close to the ceiling ($z/L=0.75$). As noted above, LES predicts a complicated patch of activity close to the upper right corner dominated by vortical flow. The k-ϵ model, in contrast, merely predicts a decaying jet and accordingly fails to predict the turbulent patch in the corner, which is consistent with the underprediction of the level of turbulence observed in Fig. 28.

5 Conclusions

The ventilation flow inside a simple cubicle was investigated using LES with both a constant coefficient and dynamic model, and the k-ϵ model. The effect of inlet turbulence intensity has been investigated using idealized uniform mean inlet conditions with 0%, 5%, and 13% inlet turbulence intensities. It is seen that the 5% and 13% cases exhibit much faster spreading and mixing with the room air than the laminar inflow case and that the statistics predicted in these two cases are close to each other, especially far from the inlet. We conjecture that beyond a threshold level of inlet turbulence intensity, the jet develops nearly independently of the inlet turbulence intensity. This is consistent with the findings of Jiang [44], Loomans [42], and Joubert et al. [43] who likewise found little sensitivity to the inlet turbulence levels. However, the laminar inlet flow case yielded significant deviations of the mean flow and turbulence levels from the simulations with higher levels of inlet turbulence. The results of flow simulations with experimentally measured profiles for the inlet conditions are compared with those for the 13% case with uniform mean inlet profiles. It is seen that near the inlet the flow is sensitive to the inlet flow details, but these effects become less pronounced, although nonnegligible, further away from the inlet. The results of simulations using the constant coefficient Smagorinsky and the dynamic LES

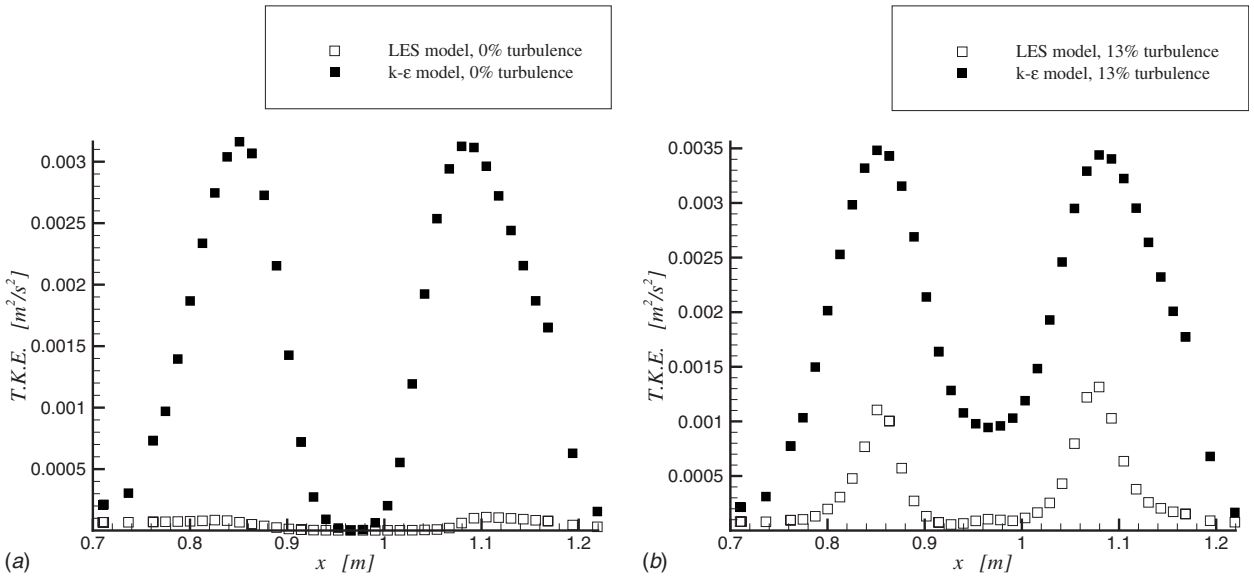

Fig. 27 Turbulent kinetic energy from k-ϵ and LES models at $z/L=-0.8$: (*a*) 0% and (*b*) 13% inlet turbulence intensities

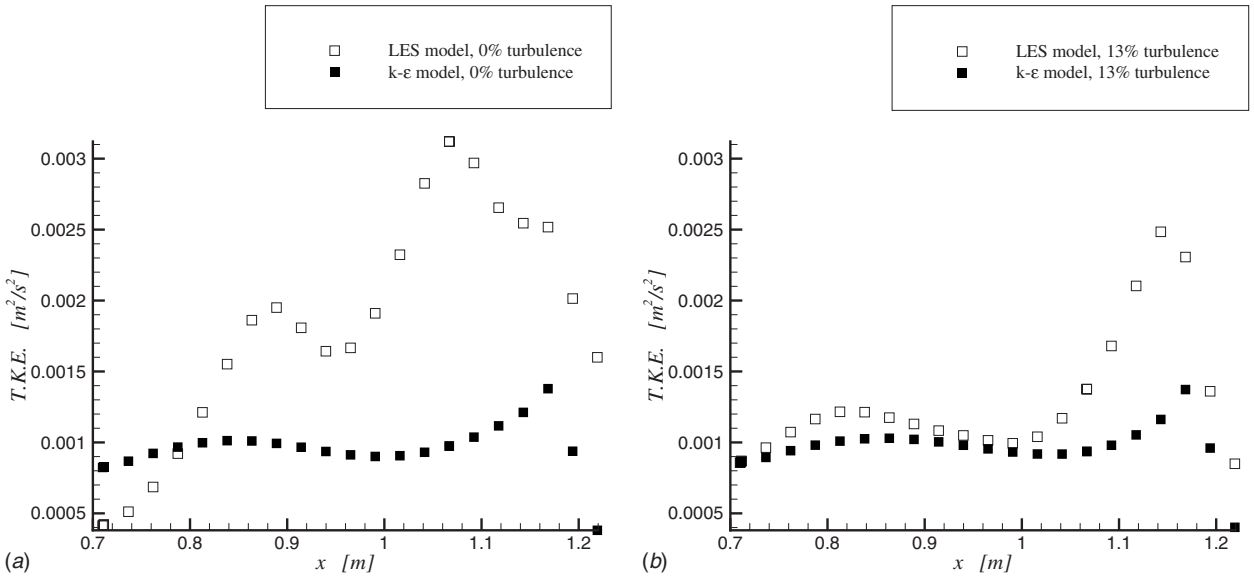

Fig. 28 Turbulent kinetic energy from k-ϵ and LES models at $z/L=0.75$: (*a*) 0% and (*b*) 13% inlet turbulence intensities

models agree reasonably well especially far from the inlet where most of the turbulent kinetic energy is resolved. The most significant differences are seen near the inlet, where the subgrid-scales' contribution to the total turbulent kinetic energy is as high as 30% of the total turbulent kinetic energy. The k-ϵ model simulations are compared at 0% and 13% inlet turbulence intensities. It is seen that the k-ϵ model is nearly insensitive to the level of inlet turbulence especially far from the inlet. Finally, the results of simulations using the k-ϵ and LES models with 0% and 13% inlet turbulence intensities are compared. It is seen that the k-ϵ model predictions for the 0% case are significantly different than the LES predictions, as the k-ϵ model fails to capture the slow spatial development of the jet into a fully turbulent state. At the 13% turbulence level, it is seen that the k-ϵ model predicts the general features of the mean velocity reasonably well. Even for this case, the k-ϵ overpredicts the spreading rate of the jet relative to the LES model and fails to capture the complicated unsteady flow pattern near the ceiling leading to significant overprediction of the turbulent kinetic near the inlet and underprediction of it near the ceiling.

Acknowledgment

This work was supported in part by the Environmental Protection Agency, through the Syracuse University NY STAR Center for Environmental Quality Systems/EPA Indoor Environmental Research Program Collaboration.

References

[1] Spengler, J. J., Samuel, J. M., and McCarthy, J. F., 2001, *Indoor Air Quality Handbook*, McGraw-Hill, New York.
[2] Pope, S. B., 2000, *Turbulent Flows*, Cambridge University Press, Cambridge.
[3] Wilcox, D. C., 2004, *Turbulence Modeling for CFD*, DCW Industries, Inc., La Canada, CA.
[4] Smagorinsky, J., 1963, "General Circulation Experiments With the Primitive Equations: I. The Basic Equations," Mon. Weather Rev., **91**, pp. 99–164.
[5] Lilly, D. K., 1967, "The Representation of Small-Scale Turbulence in Numerical Simulation Experiments," Proceedings of the IBM Scientific Computing Symposium on Environmental Sciences, IBM Form 320-1951, pp. 195–210.
[6] Deardorff, J. W., 1974, "Three-Dimensional Numerical Study of the Height and Mean Structure of a Heated Planetary Boundary Layer," Boundary-Layer Meteorol., **7**, pp. 81–106.
[7] Schumann, U., 1975, "Subgrid-Scale Model for Finite Difference Simulations of Turbulent Flows in Plane Channels and Annuli," J. Comput. Phys., **18**, pp. 376–404.
[8] Pope, S. B., 2004, "Ten Questions Concerning the Large-Eddy Simulation of Turbulent Flows," New J. Phys., **6**(35), pp. 1–24.
[9] Germano, M., Piomelli, U., Moin, P., and Cabot, W. H., 1991, "A Dynamic Subgrid-Scale Eddy Viscosity Model," Phys. Fluids A, **3**, pp. 1760–1765.
[10] Lilly, D. K., 1992, "A Proposed Modification of the Germano Subgrid-Scale Closure Method," Phys. Fluids A, **4**, pp. 633–635.
[11] Meneveau, C., Lund, T. S., and Cabot, W. H., 1996, "A Lagrangian Dynamic Subgrid-Scale Model of Turbulence," J. Fluid Mech., **319**, pp. 353–385.
[12] Nielson, P. V., Restive, A., and Whitelaw, J. H., 1978, "The Velocity Characteristics of Ventilated Room," ASME J. Fluids Eng., **100**(9), pp. 291–298.
[13] Murakami, S., Kato, S., and Suyama, Y., 1992, "Three Dimensional Numerical Simulation of Turbulent Airflow in a Ventilated Room by Means of a Two-Equation Model," ASHRAE Trans., **98**(1), pp. 82–97.
[14] Chen, Q., 1995, "Comparison of Different k-ϵ Models for Indoor Airflow Computations," Numer. Heat Transfer, Part B, **28**, pp. 353–369.
[15] Nielson, P. V., 1998, "Selection of Turbulence Models for Prediction of Room Airflow," ASHRAE Trans., **104**, pp. 1119–1127.
[16] Chen, Q., and Jiang, Z., 1992, "Significant Questions in Predicting Room Air Motion," ASHRAE Trans., **98**(1), pp. 929–939.
[17] Davidson, L., and Nielson, P. V., 1996, "Large Eddy Simulations of the Flow in Three-Dimensional Ventilated Room," Proceedings of the Fifth International Conference on Air Distribution in Rooms, Yokohama, Japan, pp. 161–168.
[18] Zhang, W., and Chen, Q., 2000, "Large Eddy Simulation of Indoor Airflow With a Filtered Dynamic Subgrid Scale Model," Int. J. Heat Mass Transfer, **43**, pp. 3219–3231.
[19] Jiang, Y., and Chen, Q., 2003, "Using Large Eddy Simulation to Study Airflows in and Around Buildings," ASHRAE Trans., **109**(2), pp. 517–526.
[20] Zhang, W., and Chen, Q., 2000, "Large Eddy Simulation of Natural and Mixed Convection Airflow Indoors With Two Simple Filtered Dynamic Subgrid Scale Models," Numer. Heat Transfer, Part A, **37**(5), pp. 447–463.
[21] Shah, K. B., and Ferziger, J. H., 1995, "A New Non-Eddy Viscosity Sub-Grid-Scale Model and Its Application to Channel Flow," *Annual Research Briefs*, Center for Turbulence Research, Stanford, CA.
[22] Zhai, Z., Zhang, Z., Zhang, W., and Chen, Q., 2007, "Evaluation of Various Turbulence Models in Predicting Airflow and Turbulence in Enclosed Environments by CFD—Part 1: Summary of Prevalent Turbulence Models," HVAC&R Res., **13**(6), pp. 853–870.
[23] Zhang, Z., Zhang, W., Zhai, Z., and Chen, Q., 2007, "Evaluation of Various Turbulence Models in Predicting Airflow and Turbulence in Enclosed Environments by CFD—Part 2: Comparison With Experimental Data From the Literature," HVAC&R Res., **13**(6), pp. 871–886.
[24] Davidson, L., Nielsen, P., and Sveningsson, A., 2003, "Modification of the v2f Model for Computing the Flow in a 3D Wall Jet," *Turbulence Heat and Mass Transfer*, K. Hanjalic, Y. Nagano, and M. J. Tummers, eds., Begell House, Inc., New York, Wallingford, UK, Vol. 213, pp. 65–72.
[25] Yakhot, V., and Orszag, S. A., 1986, "Renormalization Group Analysis of Turbulence," J. Sci. Comput., **1**, pp. 3–51.
[26] Launder, B. E., and Sharma, B. I., 1974, "Application of the Energy Dissipation Model of Turbulence to Calculation of Flow Near a Spinning Disk," Lett. Heat Mass Transfer, **1**, pp. 131–138.
[27] Durbin, P. A., 1995, "Separated Flow Computations With the k-ϵ-$v2$ Model," AIAA J., **33**, pp. 659–664.
[28] Chen, Q., and Srebric, J., 2002, "A Procedure for Verification, Validation, and Reporting of Indoor Environment CFD Analyses," HVAC&R Res., **8**(2), pp. 201–216.
[29] Chen, Q., and Zhai, Z., 2004, "The Use of CFD Tools for Indoor Environmental Design," *Advanced Building Simulation*, A. Malkawi and G. Augenbroe, eds., Spon, New York, pp. 119–140.

[30] Fluent Inc., 2006, FLUENT User's Guide, NH, Lebanon.
[31] Launder, B. E., and Spalding, D. B., 1972, *Lectures in Mathematical Models of Turbulence*, Academic, New York.
[32] Wolfshtein, M., 1969, "The Velocity and Temperature Distribution of One-Dimensional Flow With Turbulence Augmentation and Pressure Gradient," Int. J. Heat Mass Transfer, **12**, pp. 301–318.
[33] Kader, B., 1981, "Temperature and Concentration Profiles in Fully Turbulent Boundary Layers," Int. J. Heat Mass Transfer, **24**(9), pp. 1541–1544.
[34] Germano, M., 1992, "Turbulence: The Filtering Approach," J. Fluid Mech., **286**, pp. 229–255.
[35] Marr, D., 2007, "Velocity Measurements in the Breathing Zone of a Moving Thermal Manikin Within the Indoor Environment," Ph.D. thesis, Syracuse University, Syracuse.
[36] Friedrich, R., and Arnal, M., 1990, "Analysing Turbulent Backward-Facing Step Flow With the Lowpass-Filtered Navier–Stokes Equations," J. Wind. Eng. Ind. Aerodyn., **35**, pp. 101–128.
[37] Le, H., Moin, P., and Kim, J., 1997, "Direct Numerical Simulation of Turbulent Flow Over a Backward-Facing Step," J. Fluid Mech., **330**, pp. 349–374.
[38] Mathey, F., Cokljat, D., Bertoglio, J. P., and Sergent, E., 2006, "Assessment of the Vortex Method for Larged Eddy Simulation Inlet Conditions," Prog. Comput. Fluid Dyn., **6**, pp. 58–67.
[39] Lee, S., Lele, S., and Moin, P., 1992, "Simulation of Spatially Evolving Turbulence and the Applicability of Taylor's Hypothesis in Compressible Flow," Phys. Fluids A, **4**, pp. 1521–1530.
[40] Smirnov, A., Shi, S., and Celik, I., 2001, "Random Flow Generation Technique for Large Eddy Simulation and Particle Dynamics Modeling," ASME J. Fluids Eng., **123**, pp. 359–371.
[41] Mathey, F., Cokljat, D., Bertoglio, J. P., and Sergent, E., 2003, "Specification of LES Inlet Boundary Condition Using Vortex Method," *Fourth International Symposium on Turbulence, Heat and Mass Transfer*, K. Hanjalić, Y. Nagano, and M. Tummers, eds., Begell House, Inc., Antalya, Turkey.
[42] Loomans, M., 1998, "The Measurement and Simulation of Indoor Air Flow," Ph.D. thesis, Eindhoven University of Technology, Eindhoven, The Netherlands.
[43] Joubert, P., Sandu, A., Beghein, C., and Allard, F., 1996, "Numerical Study of the Influence of Inlet Boundary Conditions on the Air Movement in a Ventilated Enclosure," Proceedings of the Roomvent, Yokohama, Japan, Vol. 1, pp. 235–242.
[44] Jiang, J., 2007, "Experimental and Numerical Study of Air Flows in a Full-Scale Room," Ph.D. thesis, University of Illinois at Urbana-Champaign, Urbana.
[45] Marr, D., 2007, private communication.